Copyright
by
Cyrus Farrokh Bharucha
1997

EXPERIMENTS IN DYNAMICAL LOCALIZATION OF ULTRA-COLD SODIUM ATOMS USING TIME-DEPENDENT OPTICAL POTENTIALS

by

CYRUS FARROKH BHARUCHA, B.S., B.A., M.A.

DISSERTATION

Presented to the Faculty of the Graduate School of

The University of Texas at Austin

in Partial Fulfillment

of the Requirements

for the Degree of

DOCTOR OF PHILOSOPHY

THE UNIVERSITY OF TEXAS AT AUSTIN

August 1997

EXPERIMENTS IN DYNAMICAL LOCALIZATION OF ULTRA-COLD SODIUM ATOMS USING TIME-DEPENDENT OPTICAL POTENTIALS

APPROVED BY
DISSERTATION COMMITTEE:

Supervisor: _____

_____

_____

_____

_____

_____

To Laju and Farrokh Bharucha.

Thank you, mom and dad, for all the encouragement and love.

Acknowledgements

I have had the very good fortune of working on my graduate research in Mark Raizen's Atom Optics Laboratory at the University of Texas at Austin. Mark is an energetic scientist with a contagious enthusiasm for physics. He has a broad knowledge of the interesting questions in modern physics and an inspiring ability to propose illuminating and realizable experiments to answer them. Moreover, he engenders this same creativity in his graduate students. The nurturing but challenging atmosphere he fosters in his lab has made it an enjoyable and rewarding venue for research. It has been an honor and a pleasure to work with Mark and the other bright physicists in his group.

Paul Williams, a postdoctoral fellow in the lab's early crew, helped design and build our experiments on the modulated system. Paul also wrote the original versions of programs used in simulating our experimental conditions. Another postdoctoral fellow, Fred Moore, taught me numerous valuable techniques of laboratory physics. In addition to being a superb experimentalist, Fred has an amazing ability to explain the most intricate physical problems with the simplest of symmetry principles. He also has a Feynman-esque sense of mischievous humor that added an entertaining dash of bizzareness to the lab's personality. I had the pleasure of working with Mark, Fred, Paul, and John Robinson on our first experiments in quantum chaos [1, 2, 3, 4, 5], which are the subject of this dissertation.

John was Mark's first graduate student, and he built a large part of the the lab's infrastructure in its early days. John was a major force in making our early experiments happen, and further details and descriptions of this work can be found in his dissertation [6]. He is a unending source of information and know-how on many subjects; I owe him a sincere thanks for hours of stimulating discussions on topics ranging from atmospheric optics to Zeeman shifts. John is a terrific person to work with, and I have very fond memories of aligning optics and deriving equations with him during my first years in the lab. Later, I also had the pleasure of teaming with Kirk Madison, a master at experimental design and computer control. Kirk and I worked on several experiments together and I was lucky to have a companion with his wit and endurance when things did not work as planned. Kirk stayed up with me through many nights to bask in the warm glow of oscilloscope traces representing fresh new data while the sun rose outside. Mark, Kirk, and I worked with super-Marine Steve Wilkinson, laserjock extraordinaire Pat Morrow, and culinary master Martin Fischer on our recent experiments in quantum transport [7, 8, 9, 10]. Martin is a talented experimentalist with a knack for building laboratory instruments and getting them to behave. He contributed to the work described in this dissertation by spearheading the design and construction of the home-built dye laser that supplied the interaction potential for these experiments [11].

Bala Sundaram and Qian Niu have been strongly involved with the theoretical and numerical analyses of many of the group's experiments, and the lab has benefited greatly from fruitful collaborations with them and with Qian's graduate students Georgios Georgakis and Bob Jahnke. Bala, a theorist

with a good eye for experimentally testable ideas, has my gratitude for many enlightening discussions on nonlinear dynamics, sociology, and career decisions for a young physicist. A true renaissance man, he is a rich source of knowledge on many topics lying within the broad field of physics, and on many more lying outside it. Georgios, my flying buddy, encouraged me long ago to follow my heart and add a physics major. I thank him dearly for that valuable advice, and for all his insights on numerical techniques [12], finance, teaching, dancing, and writing good patent applications.

For me, an important aspect of graduate study has been the inquisitive conversations I have had with my colleagues in our efforts to understand basic physical concepts that at first glance appear to be elementary. I am deeply grateful to my fellow graduate students (and friends) John, Georgios, Pat, Martin, Kirk, Bruce Klappauf, Dan Steck, and Windell Oskay for the many times they have joined me over coffee, chocolate, pizza, or gourmet Thai cooking to discuss the way the world spins.

Les Deavers, Jim Pinget, John England, and Ed McKnight from the Physics Department's Mechanical Section have helped me often in various aspects of the construction of our apparatus. Thanks also go to Jan Dunn, Norma Kotz, Glenn Suchan, and Olga Vorloou for making daily life in a large department run so smoothly.

I am grateful to my friends outside the lab for making these six years in Austin so enjoyable. Diana Ballard, Alex Barr, Mike Burns, Phillip Bryan, Verena Fischer, Georgie Georgakis, Arturo Morosoff, Elda Treviño Flores, and

Joe White have my heartfelt thanks for just plain being there.

For all their efforts in helping me in the final editing of this dissertation, I heartily thank Mark, Bruce, Dan, John, Kirk, Martin, Mike, and Windell.

Mom, Dad, and Jyoti - my love and gratitude to you for all your support and caring.

EXPERIMENTS IN DYNAMICAL LOCALIZATION OF ULTRA-COLD SODIUM ATOMS USING TIME-DEPENDENT OPTICAL POTENTIALS

Publication No. _____

Cyrus Farrokh Bharucha, Ph.D.
The University of Texas at Austin, 1997

Supervisor: Mark Raizen

This dissertation describes our work with time-dependent dipole potentials on the roles of classical and quantum dynamics in atom optics. We measure momentum transfer in parameter regimes for which the classical dynamics are chaotic, and we observe a wide range of phenomena. These phenomena include classical mechanisms such as the resonance overlap criterion for global stochasticity as well as the quantum suppression of chaos by dynamical localization. The high degree of control over the experimental parameters enables detailed comparisons with theoretical predictions and opens new avenues for investigating theories in quantum chaos.

Table of Contents

Acknowledgements **v**

Abstract **ix**

List of Figures **xii**

Chapter 1. Introduction **1**

Chapter 2. Background: A Two-Level Atom in a Standing-Wave Potential **3**

Chapter 3. Experimental Method **11**
3.1 Initial Conditions 11
3.2 Interaction Potential 14
3.3 Measurement of the Atomic Momentum 16

Chapter 4. Resonance Overlap in a Single-Pulse Interaction **25**
4.1 Introduction 25
4.2 Experimental Apparatus 26
4.3 The Resonance Overlap Criterion 27
4.4 Experimental Results 29

Chapter 5. The Kicked Rotor **34**
5.1 Introduction 34
5.2 Classical Predictions and Consequences of the Finite Pulse Duration 37
5.3 Quantum Predictions 40
5.4 Experimental Parameters 43
5.5 Experimental Results 48
5.6 Quantum Resonances 50

Chapter 6. The Modulated Standing Wave **57**
6.1 Introduction 57
6.2 Experimental Apparatus 57
6.3 Classical Analysis 58
6.4 Experimental Results: Quantum Mechanical Effects 62

Chapter 7. Future Directions **70**

Bibliography **71**

Vita **75**

List of Figures

2.1 Poincaré surface of section for a single resonance. 10

3.1 Schematic of the lasers and frequency control systems. 19
3.2 Beam configurations for the experiments. 20
3.3 RMS spatial width as a function of free drift time. 21
3.4 Timing diagram for various events in the experimental procedure. 22
3.5 Two-dimensional atomic distributions after free expansion. . . . 23
3.6 One-dimensional atomic momentum distributions. 24

4.1 Poincaré surface of section for the $\sin^2$ potential. 31
4.2 Poincaré surface of section for the $\sin^2$ interaction with a value of V_o leading to resonance overlap. 32
4.3 RMS momentum for $\sin^2$ and square pulses. 33

5.1 Digitized temporal profile of the pulse train. 52
5.2 Poincaré surface of section for the kicked rotor. 53
5.3 Experimental time evolution of the momentum distribution for the kicked rotor. 54
5.4 Energy $\langle (p/2\hbar k_L)^2 \rangle /2$ as a function of the number of kicks. . . . 55
5.5 Experimental observation of quantum resonances. 56

6.1 Simulation of resonant kicks. 66
6.2 RMS momentum width as a function of the modulation amplitude λ. 67
6.3 Bessel functions. 68
6.4 Poincaré surfaces of section and momentum distributions for the modulated system. 69

Chapter 1

Introduction

The past few years have seen a resurgence in the use of classical mechanics in the description of strongly perturbed and strongly coupled quantum systems in atomic physics [13, 14], where the traditional perturbative treatment of the Schrödinger equation breaks down. In particular, recent advances in classical nonlinear dynamics and chaos have had important applications in the description of the photo-absorption spectrum of Rydberg atoms in strong magnetic fields [15], the microwave ionization of highly excited hydrogen atoms [16], and the excitation of doubly excited states of helium atoms [17]. These examples together with recent work on mesoscopic systems [18] explore classical-quantum correspondence in situations where the classical limit exhibits chaos, an area of study referred to as "quantum chaos" [19].

Parallel developments in laser cooling and trapping techniques has led in recent years to spectacular advances in the manipulation and control of atomic motion [20]. At the ultra-cold temperatures that are now attainable, the wave nature of atoms becomes important. These advances have lead to the development of the new field of atom optics [21]. Until recently, the primary focus in atom optics has been the development of optical elements such as atomic mirrors, beamsplitters and lenses for atomic de Broglie waves. Our work, reviewed

in this dissertation, has emphasized the novel regime of time-dependent potentials and hence dynamics in atom optics. In particular, we study momentum distributions of ultra-cold atoms exposed to time-dependent, one-dimensional, optical dipole forces that are typically highly nonlinear. Thus, the classical motion can become chaotic. As dissipation can be made negligibly small in this system, quantum effects can become important. Our work has established that these features together make atom optics a simple and controlled setting for the experimental study of quantum chaos [5].

As this work deals with momentum transfer from light to atoms, it is important to review some basic concepts. The relevant unit of momentum is one photon recoil ($\hbar k_L$), the momentum change experienced by an atom when it absorbs or emits a photon. For sodium atoms, this velocity change is 3 cm/s. The desired process for atom optics is stimulated scattering, where the atom remains in the ground state and coherently scatters the photon in the direction of the incident laser beam. Spontaneous scattering, on the other hand, is a dissipative process and must be minimized. In a single beam (traveling wave), the atom scatters coherently in the forward direction and there is no net momentum transfer. However in a standing wave of light, created by the superposition of two counter-propagating beams, the atom can also back-scatter. This process leads to a momentum change of two photon recoils, or a 6 cm/s velocity change for sodium. The effective dipole potential that the atom experiences scales with intensity (irradiance) I and detuning δ_L from atomic resonance as I/δ_L while spontaneous scattering varies as I/δ_L^2 [22]. Therefore, by detuning further from resonance, it is possible to make the probability of spontaneous scattering negligible, while still having a substantial dipole potential.

Chapter 2

Background: A Two-Level Atom in a Standing-Wave Potential

In the experiments presented here, we subject our atoms to time-dependent, one-dimensional optical dipole forces created by a pair of counter-propagating laser beams. How does one understand the interaction between these beams and the sample of atoms?

Consider a two-level atom of transition frequency ω_o interacting with a standing wave of near-resonant light. If the standing wave is composed of two counter-propagating beams, each with field amplitude E_o and wavenumber $k_L = 2\pi/\lambda_L = \omega_L/c$, then the atom is exposed to an electric field of the form $\vec{E}(x,t) = \hat{y}[E_o \cos(k_L x)e^{-i\omega_L t} + c.c.]$ and its Hamiltonian in the rotating-wave approximation is given by

$$H(x,p,t) = \frac{p^2}{2M} + \hbar\omega_o|e\rangle\langle e| + \left[\mu E_o \cos(k_L x)e^{-i\omega_L t}|e\rangle\langle g| + H.c.\right] \ . \qquad (2.1)$$

Here $|g\rangle$ and $|e\rangle$ are the ground and excited internal states of the atom, x and p are its center of mass position and momentum, M is its mass, and μ is the dipole moment coupling the internal states.

The wavefunction for this atom can be written in the position representation as $|\psi\rangle = \psi_g(x,t)|g\rangle + \psi_e(x,t)e^{-i\omega_L t}|e\rangle$; it evolves according to the

Schrödinger equation $(i\hbar\partial/\partial t)|\psi\rangle = H|\psi\rangle$. By combining these two equations with Eq. 2.1 and then operating from the left with $\langle g|$ we get an expression for the evolution of the ground state amplitude

$$i\hbar\frac{\partial\psi_g(x,t)}{\partial t} = -\frac{\hbar^2}{2M}\frac{\partial^2}{\partial x^2}\psi_g(x,t) + \frac{\hbar\Omega}{2}\cos(k_L x)\psi_e(x,t)\ , \tag{2.2}$$

where $\Omega/2 \equiv \mu E_o/\hbar$ is the Rabi frequency of an atom interacting with just one of the light beams. Similarly, by operating from the left with $\langle e|$, we get

$$i\hbar\frac{\partial\psi_e(x,t)}{\partial t} = -\frac{\hbar^2}{2M}\frac{\partial^2}{\partial x^2}\psi_e(x,t) + \frac{\hbar\Omega}{2}\cos(k_L x)\psi_g(x,t) + \hbar\delta_L\psi_e(x,t)\ . \tag{2.3}$$

Here spontaneous emission from the excited state is neglected; this approximation is valid for the case of large detunings $\delta_L \equiv \omega_o - \omega_L$ from the atomic resonance. The large detuning also permits an adiabatic elimination of the excited state amplitude; for sufficiently large detuning the excited state amplitude can be neglected and the atom remains in the ground state. In this regime the two derivative terms of Eq. 2.3 are small compared to $\hbar\delta_L\psi_e$, and the two equations can be decoupled into a single equation for the ground state amplitude:

$$i\hbar\frac{\partial\psi_g}{\partial t} = -\frac{\hbar^2}{2M}\frac{\partial^2}{\partial x^2}\psi_g + \frac{\hbar\Omega^2}{4\delta_L}\cos^2(k_L x)\psi_g\ . \tag{2.4}$$

This has the form of a Schrödinger equation $i\hbar\partial\Psi(x,t)/\partial t = H\Psi(x,t)$ with a Hamiltonian

$$H(x,p,t) = \frac{p^2}{2M} - V_o\cos 2k_L x\ . \tag{2.5}$$

A uniform potential offset from Eq. 2.4 has been dropped here by shifting the phase of the wavefunction: $\Psi \equiv \exp(i\Omega^2 t/8)\psi_g$. Equation 2.5 describes a point particle in a one-dimensional sinusoidal potential. The potential has a period

of one-half the optical wavelength and an amplitude V_o that is proportional to the intensity of the standing-wave and inversely proportional to its detuning:

$$\begin{aligned} V_o &= \frac{\hbar\Omega^2}{8\delta_L} \\ &= \frac{I}{\hbar\delta_L c\epsilon_o}\,\mu^2 \\ &= \frac{I}{\hbar\delta_L c\epsilon_o}\,\frac{2}{3}\,\frac{3\pi\Gamma\epsilon_o\hbar c^3}{\omega_o^3} \\ &= \frac{2}{3}\,\frac{\hbar(\Gamma/2)^2}{\delta_L}\,\frac{I}{I_{sat}}\,. \end{aligned} \tag{2.6}$$

Here Γ is the linewidth of the transition and μ is its dipole matrix element. I is the intensity (irradiance) of each of the beams comprising the standing wave and $I_{sat} \equiv \pi\hbar\omega_o\Gamma/3\lambda_L^2 = 6$ mW/cm^2 is the saturation intensity for the transition. Equation 2.6 was derived for a standing wave composed of two counterpropagating beams of equal intensities. If the two beams are not perfectly matched the potential amplitude is still given by this equation, with I taken as the geometric mean of the two intensities.

The classical analysis of Eq. 2.5 is the same as for a pendulum or rotor, except that the conjugate variables are position and momentum rather than angle and angular momentum. A Poincaré surface of section for this system is shown in Fig. 2.1. The position coordinate is shown for one period of the standing wave. This is a textbook system with a stable fixed point at the center corresponding to the bottom of the potential well, and an unstable fixed point corresponding to the top. The closed orbits represent oscillatory motion for particles with energy less than the total well depth $2V_o$, while the continuing paths describe the unconfined motion of higher-energy particles.

The sinusoidal potential of the pendulum equation is a starting point in

the study of nonlinear dynamics. The optical system represented by Eq. 2.5 is a valuable realization of this one-dimensional Hamiltonian. Unlike the periodic potentials in condensed matter systems, this realization is effectively free from dissipation mechanisms such as phonon scattering and imperfections in the lattice periodicity.

We can exploit the control available in the experiment on the optical standing wave to achieve more interesting systems. By adding a time dependence to the laser intensity, we can vary the amplitude of the potential as a function of time. By differentially shifting the optical frequencies of the beams that compose the standing wave, we can also vary its position (or phase) in time. With these considerations, we see that the electric field of the standing wave takes the form $\vec{E}(x,t) = \hat{y}[E_o F_1(t)\cos\{k_L[x - F_2(t)]\}e^{-i\omega_L t} + c.c.]$. The time scales for these controls ranged between $\sim$ 25 ns (the response time of our optical modulators) and milliseconds (the duration of the experiments). The amplitude and phase modulations were therefore slow compared to the parameters ω_o and δ_L relevant to the derivation of Eq. 2.5, so they change that equation by simply modifying the amplitude and phase of the sinusoidal potential. The generic time-dependent potential is thus

$$H(x,p,t) = \frac{p^2}{2M} + V_o F_{amp}(t)\cos\left[2k_L x - F_{ph}(t)\right] \ . \tag{2.7}$$

In our experiment we expose sodium atoms to a standing wave of light that is near-resonant to the D_2 transition with $\lambda_L = 589$ nm. To what extent is Eq. 2.7 a good representation of a sodium atom exposed to an optical standing wave in the laboratory? The two-level atom and rotating-wave approximations are well justified for this optical-frequency transition. The adiabatic elimina-

tion of the excited-state amplitude is appropriate for detunings that are large compared to the linewidth Γ and to the recoil shift frequency ω_r, both of which are characteristics of the atomic transition. For the sodium D_2 transition the values for these quantities are

$$\frac{\Gamma}{2\pi} = 10 \text{ MHz} \tag{2.8}$$

and

$$\frac{\omega_r}{2\pi} \equiv \frac{1}{2\pi}\frac{\hbar k_L^2}{2M} = 25 \text{ kHz}. \tag{2.9}$$

Our detunings of several GHz placed the experiment well within this regime. It is also important to note that for the sodium D_2 transition in linearly polarized light, the light shift is the same for all the m_F sublevels.

The one-dimensional nature of Eq. 2.7 comes from the assumption that the laser beams have spatially uniform transverse profiles. In these experiments the width of the atomic cloud ($\sigma_{xo} \sim 0.15$ mm RMS) during the illumination by the standing wave was small compared to the width of the laser profile (which had a $1/e$ field waist of $w_o \sim 1.9$ mm), so the transverse variations in the potential were small.

The periodicity of this potential is limited only by the coherence length of the laser that produces it. Since this length is large compared to the difference in optical pathlength taken by the two beams that make up the standing wave, the potential has a coherent periodic structure over the entire spatial extent of the atomic sample.

For simulations [23] and theoretical analyses it is helpful to write Eq. 2.7 in dimensionless units. We take $x_u = 1/2k_L$ to be the basic unit of distance, so the dimensionless variable $\phi \equiv x/x_u = 2k_L x$ is a measure of the atom's position

along the standing-wave axis. Depending on the time dependence of the interaction, an appropriate time scale t_u is chosen as the unit of time; the variable $\tau \equiv t/t_u$ is then a measure of time in this unit. The atomic momentum is scaled accordingly into the dimensionless variable $\rho \equiv p\, t_u/Mx_u = p\, 2k_L t_u/M$. This transformation preserves the form of Hamilton's equations with a new (dimensionless) Hamiltonian $\mathcal{H}(\phi, \rho, \tau) = H(x, p, t) \cdot t_u^2/Mx_u^2 = H \cdot 8\omega_r t_u^2/\hbar$.

With this scaling, Eq. 2.7 can be written in the dimensionless form

$$\mathcal{H}(\phi, \rho, \tau) = \frac{\rho^2}{2} + k f_{amp}(\tau) \cos\left[\phi - f_{ph}(\tau)\right] \ , \tag{2.10}$$

where the variables τ, ϕ, and ρ are dimensionless measures of time, displacement along the standing wave, and the atomic momentum:

$$\begin{aligned} \tau &= t/t_u \ , \\ \phi &= 2k_L x \ , \\ \rho &= p\, 2k_L t_u/M \ . \end{aligned} \tag{2.11}$$

The scaled potential amplitude here is $k \equiv V_o \cdot 8\omega_r t_u^2/\hbar$. In these transformed variables, the Schrödinger equation in the position representation becomes

$$i\hbar\frac{\partial}{\partial\tau}\Psi(\phi, \tau) = \left[-\frac{\hbar^2}{2}\frac{\partial^2}{\partial\phi^2} + k f_{amp}(\tau) \cos\left[\phi - f_{ph}(\tau)\right]\right] \Psi(\phi, \tau) \ . \tag{2.12}$$

Here the dimensionless parameter $\hbar$ depends on the temporal scaling used in the transformation

$$\hbar \equiv 8\omega_r t_u \ . \tag{2.13}$$

As with the classical analyses of this system, the quantum analysis is similar to that of a pendulum. In the quantum picture there is a distinction between our system and a pendulum. Because of its periodic boundary

conditions, a pendulum's wavefunction has the same spatial periodicity as its potential. Since an atom in the optical potential can be localized in space, its wavefunction does not have this imposed periodicity.

In the transformation outlined here, the commutation relation between momentum and position becomes $[\phi, \rho] = i\hbar$. Thus $\hbar$ is a measure of the quantum resolution in the transformed phase-space. Another general note on this transformation concerns the measure of the atomic momentum. Since an atom interacts with a near-resonant standing wave, its momentum can be changed by stimulated scattering of photons in the two counter-propagating beams. If a photon is scattered from one of these beams back into the same beam, the result is no net change in the atom's momentum. But if the atom scatters a photon from one of the beams into the other, the net change in its momentum is two photon recoils. The atom can thus exchange momentum with the standing wave only in units of $2\hbar k_L = 2$ recoils $= 6$ cm/s $\cdot M$. The momentum is naturally measured in this unit of momentum transfer. In the transformed, dimensionless units, this quantity is

$$\frac{p}{2\hbar k_L} = \frac{\rho}{\hbar} \, . \tag{2.14}$$

For a sample of atoms initially confined to a momentum distribution narrower than one recoil, the discreteness of the momentum transfer would result in a ladder of equally spaced momentum states. In our experiments the initial momentum distributions were significantly wider than two recoils ($\sigma_{po}/2\hbar k_L \sim 2.3$), so the observed final momenta had smooth distributions rather than discrete structures.

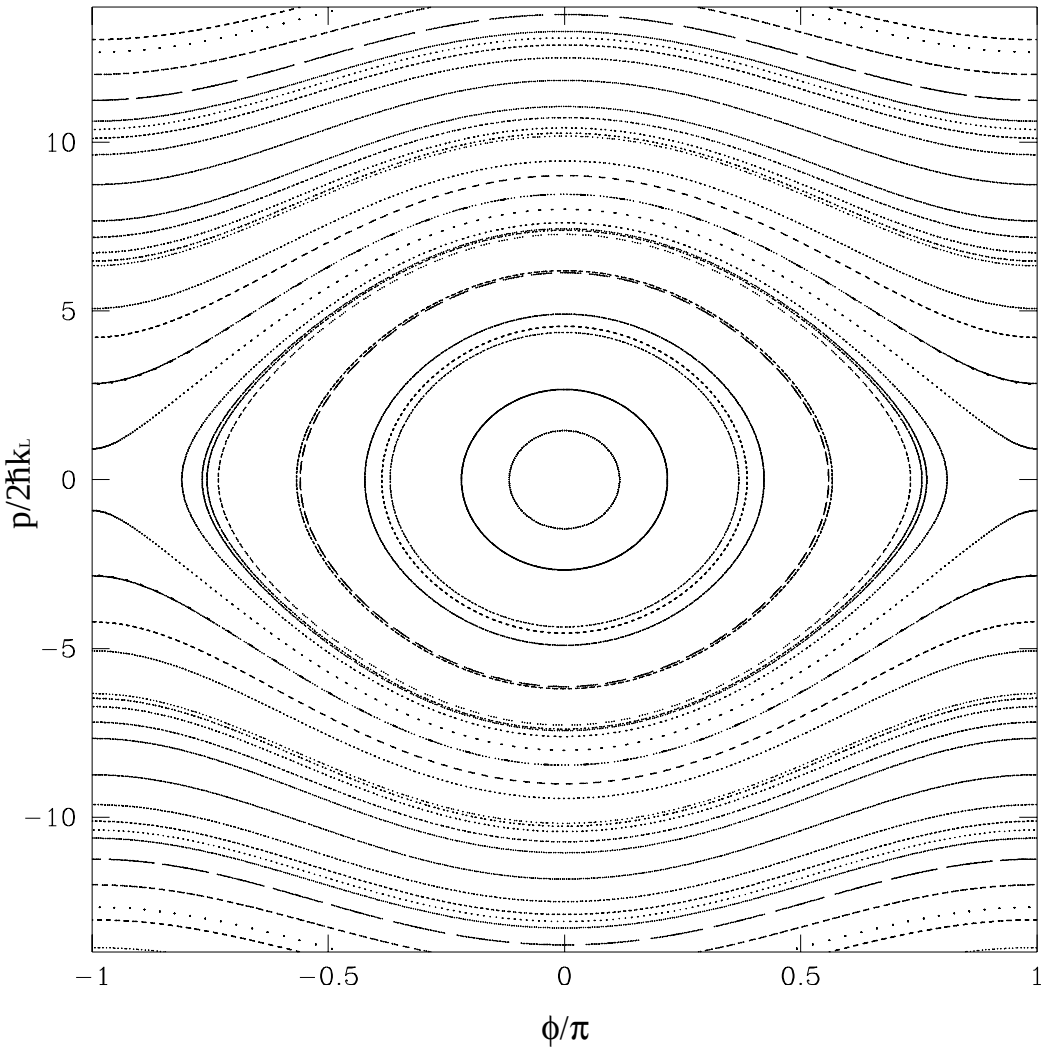

Figure 2.1: Poincaré surface of section for a single resonance. Momentum and position are in the dimensionless units defined in the text.

Chapter 3

Experimental Method

The experimental study of momentum transfer in time-dependent interactions consists of three important components: the initial conditions, the interaction potential, and the measurement of atomic momentum. The initial distribution ideally should be narrow in position and momentum, and should be sufficiently dilute so that atom-atom interactions can be neglected. The time-dependent potential should be one-dimensional, for simplicity, with full control over the amplitude and phase. In addition, noise must be minimized to enable the study of quantum effects. Finally, the measurement of final momenta after the interaction should be highly sensitive and accurate. It is possible to realize all these conditions using the techniques of laser cooling and trapping. This chapter describes the apparatus and techniques used in our experiments. Further details on the realization of these experiments can be found in [6].

3.1 Initial Conditions

Our initial conditions were a sample of ultra-cold sodium atoms that were trapped and laser-cooled in a magneto-optic trap (MOT) [20, 24]. The atoms were contained in a glass ultra-high-vacuum cell at room temperature. This cell was attached to a larger stainless steel chamber connected to a 20 l/s

ion pump. The source of atoms was a small sodium ampoule contained in a copper tube attached to the chamber. The ampoule was crushed to expose the sodium. Although the partial pressure of sodium at room temperature is below 10^{-10} Torr, there were enough atoms in the low-velocity tail of the thermal distribution to sufficiently fill the trap. The trap was formed using three pairs of counter-propagating, circularly polarized laser beams with diameters of roughly 2 cm. These beams intersected in the center of the glass cell, together with a magnetic field gradient provided by current-carrying wires arranged in an anti-Helmholtz configuration. This $\sigma^+ - \sigma^-$ configuration is standard and is used in many laboratories.

As shown in shown in Fig. 3.1, a Coherent 899-21 dye laser supplied the MOT beams. A NIST wavemeter with a resolution of 50 MHz and a scanning Fabry-Perot cavity (indicated by Monitor Cavity in the figure) aided in the initial coarse tuning of this laser. The laser was then locked by saturated absorption FM spectroscopy to a frequency 65 MHz to the blue of the $(3S_{1/2}, F = 2) \longrightarrow (3P_{3/2}, F = 3)$ sodium transition at $\lambda_L = 2\pi/k_L = 589$ nm. Note that since an acousto-optic modulator (AOM1) subsequently downshifts this beam by 80 MHz, the light incident on the atoms was 15 MHz to the red of the transition. As the atoms cycle in this transition, they can be lost to the $(3S_{1/2}, F = 1)$ ground state with a decay time that we measured as roughly 30 μs. To prevent this loss, some of the optical power was shifted into sidebands at 1.712 GHz. The higher-frequency sideband served to repump atoms from the $(3S_{1/2}, F = 1)$ state up to $(3P_{3/2}, F = 2)$, from where they could re-enter the cycling transition. These sidebands were generated by an electro-optic modulator (EOM1). This device was a 3 mm x 3 mm x 25.4 mm $LiTaO_3$

crystal from Crystal Technology, around which we built a split-ring cylindrical resonator. With 28 dBm of applied power it could modulate the light so that the first-order sidebands each had 50% as much power as the fundamental, but we found that 15% sidebands were optimal for a cold MOT.

The acousto-optic modulator AOM1 provided a mechanism for turning on and off the MOT light by diffracting it into a series of deflected modes; only the first-order downshifted mode was transmitted to the atoms in the vacuum cell. This downshifted light was monitored continuously on a photodiode (Power Lock PD) whose signal provided feedback to AOM1; thus AOM1 also served to lock the intensity of the MOT beams. The residual fluctuations were less than 1% of the average intensity.

To spatially filter the MOT light, we then coupled it into a single-mode polarization-preserving fiber. This fiber also divided the optical alignment of the experiment into two independent regions; the frequency-conditioning elements upstream of the fiber could all be optimized without affecting the alignment of the downstream beamsplitters, mirrors, waveplates, and apertures that trained the light onto the atoms in the vacuum cell. These downstream elements split the light into 6 beams, each of which had a diameter of 2 cm and a uniform intensity of typically 2 to 5 mW/cm^2.

Using this scheme, we trapped approximately 10^5 atoms into a cloud that had a Gaussian distribution in position with an RMS width of $\sigma_{xo} =$ 0.12–0.17 mm. The atoms also had a Gaussian distribution in momentum, with a spread of $\sigma_{po} = 4.6 - 6\hbar k_L$, corresponding to a temperature $50-90$ μK. This confined, cold distribution defined the initial conditions of the atoms before they were exposed to the interaction potential.

3.2 Interaction Potential

A second dye laser (the home-built laser in Fig. 3.1) provided the optical standing wave that formed the interaction potential. This laser was typically tuned 5 GHz red of resonance. Different beam configurations were used in the experiments described here, with acousto-optic and electro-optic modulators controlling the time-dependent amplitude and phase.

Figure 3.2(a) shows the configuration for the modulated standing wave experiment. An acousto-optic modulator (AOM3 in the figure) turned the interaction potential on and off with a 10%-90% switching time of 25 ns. The beam's power was monitored on a photodiode (PD1). The light was then split into a pair of spatially filtered beams that overlapped to form a standing wave intersecting the trapped atoms in the vacuum cell. These beams were considerably wider than the distribution of atoms, with typical waists of 1.9 mm. An electro-optic modulator (EOM3) shifted the phase of one of the beams, and hence the position of the standing wave along its axis. The magnitude of this shift was determined by inserting the Mach-Zehnder interferometer indicated by the dashed lines in Fig. 3.2(a) and analyzing the PM sidebands in the heterodyne signal on photodiode PD2 as described in Chapter 6. The velocity of the standing wave in the lab frame also could be varied by introducing a differential frequency shift between the two beams with two more acousto-optic modulators (AOM4 and AOM5).

For the single-pulse interaction and delta-kicked rotor experiments described in Chapters 4 and 5, a simpler configuration was used. In these experiments, the position of the standing wave was fixed, and the amplitude was varied to produce the time-dependent interactions. The configuration for these

experiments is depicted in Fig. 3.2(b). The standing wave was formed here by training the beam directly onto the atomic sample and retro-reflecting the beam with mirror M2, effectively doubling the available power while providing a fixed node in the standing wave at the surface of the retro-reflecting mirror. The initial element (AOM6) is an acousto-optic modulator that can diffract 80% of the optical power into the first-order spot. This fast modulator, with a 10% to 90% rise time of 25 ns, provided the amplitude modulation of the interaction beam. The next acousto-optic modulator (AOM7) provided additional amplitude control for preliminary experiments in which we studied the effects of amplitude noise on the dynamics. Photodiode PD1 monitored the pulse profiles during the experiments. These profiles were digitized and stored for later analyses. To measure the phase stability of the standing wave, a Michelson interferometer was constructed by inserting a beam splitter as shown by the dashed marks in Fig. 3.2(b). This measurement indicated that the standing-wave phase at the atomic sample was stable to within a few percent of a period for times up to 100 μs.

In general, it was desirable to draw as much power as possible from this laser. The amplitude of the interaction potential varies directly with its intensity and inversely with its detuning from the atomic resonance. Since the probability of spontaneous emission has a Lorentzian dependence on the detuning from resonance, this dissipative effect can be reduced by increasing the laser detuning. Raising the laser intensity by the corresponding amount allows the amplitude of the interaction potential to remain fixed. In our experiments, we had typical laser powers of $0.7 - 1.2$ W at the laser head. Subsequent modulating, shifting, and filtering in the different experiments led to powers of

$200 - 500$ mW at the atomic sample.

3.3 Measurement of the Atomic Momentum

Our original vision of these experiments involved an atomic beam whose transverse momentum distribution would be affected by interactions with the standing wave. The interactions could then be characterized by observing the transverse spatial distribution of the atomic beam some distance after it had passed through the standing wave. A very important simplification in the design of these experiments was the formulation of an alternative scheme for measuring the momentum transferred to the atoms from the standing wave.

The method we developed to make this measurement greatly simplified the data collection and obviated the need for an atomic beam altogether. After being exposed to the interaction potential in our experiments, the atoms had a new momentum distribution, but the duration of the interactions was short enough that their spatial distribution remained essentially unchanged. They were then allowed to drift in the dark for a controlled duration t_{drift} of a few milliseconds. During this time, the atoms underwent ballistic motion and their momentum distribution resulted in a widened spatial distribution. At this point we measured the spatial distribution of the atoms. Their motion was frozen by turning on the optical trapping beams in zero magnetic field to form optical molasses [20]. Under these conditions of "freezing molasses" the atoms' motion is rapidly damped, and for short times (tens of ms) their motion is negligible in comparison to the dimensions of the cloud. This damping is described in Fig. 3.3 which shows the spatial width of a sample of atoms after different drift times and exposures to the optical molasses. A charge-coupled-device (CCD)

camera was used to image the fluorescence of the atoms in this molasses. The resulting image recorded the new spatial distribution of the atoms; thus since we knew the time of flight t_{drift}, we were able to derive the atomic momentum distribution. The entire sequence of the experiment was computer-controlled.

Figure 3.4 shows the sequence of timing signals that the controlling computer generated to coordinate events in the experiment. An analog signal controlled the optical sidebands by driving an RF switch that regulated the 1.712 GHz power for EOM1. For experiments in which we used relatively small detunings, a pulse generator provided a delayed copy of this signal so there could be an adjustable optical pumping time before the trapping beams were themselves turned off. During this time (roughly 30 μs) the atoms were pumped into the $(3S_{1/2}, F = 1)$ state. Having all the atoms in this one state (rather than a mix of this and the $(3S_{1/2}, F = 2)$ state allowed a better characterization of the detuning from resonance experienced by the sample. Immediately after the trapping beams were turned off, another analog signal turned off the MOT's magnetic gradient fields. These fields remained off throughout the time the atoms were illuminated by the interaction beams, the subsequent ballistic drift time, and later when the trapping beams were turned back on to freeze the sample in optical molasses. Since the magnetic fields had a decay time of approximately 100 μs, the atoms were exposed to some residual magnetic field during the time the interaction beams were on. Although this field perturbs the internal structure of the atoms, the effect is insignificant in the calculation of the interaction potential in Eq. 2.5 because the detuning of the laser beams (GHz) is much larger than the Zeeman shifts (MHz) from the magnetic field. The computer also provided a trigger signal at the appropriate time to switch

on the interaction beams and another trigger for the CCD camera to capture the resonant fluorescence of the 'frozen' sample.

In Fig. 3.5, typical 2-D images of atomic fluorescence are shown. In Fig. 3.5(a) the initial MOT was released, and the motion was frozen after a 2 ms free-drift time. The distribution of momentum in Fig. 3.5(a) is Gaussian in both the horizontal and vertical directions. The vertical direction was integrated to give a one-dimensional distribution as shown in Fig. 3.6(a). In Fig. 3.5(b), the atoms were exposed to a particular time-dependent potential. The vertical distribution remains Gaussian, but the horizontal distribution becomes exponentially localized in this case due to the interaction potential, as shown in Fig. 3.6(b). The significance of this momentum distribution and other characteristics are analyzed in the following Chapters.

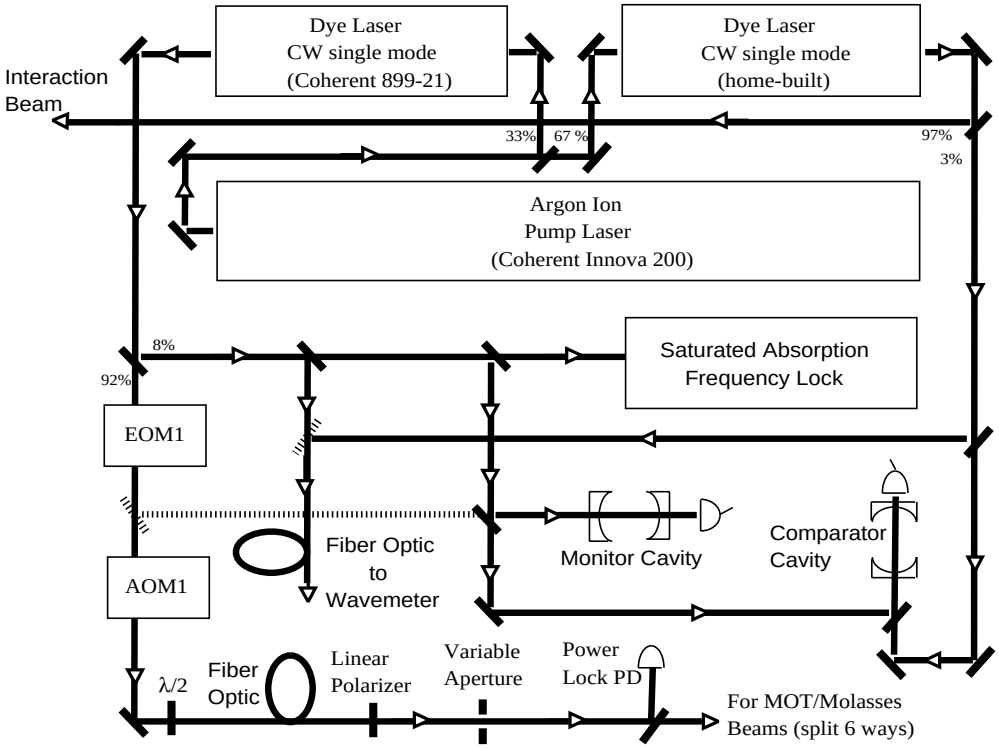

Figure 3.1: Schematic of the lasers and frequency control systems. A dye-jet laser with an argon-ion pump supplies the light for the magneto-optic trap (MOT) and optical molasses beams. A second dye laser provides the far-detuned interaction beam for the standing-wave potentials. The acousto-optic modulators (AOM) are used for frequency shifts and as fast shutters while the electro-optic modulators (EOM) are used as phase shifters and frequency modulators.

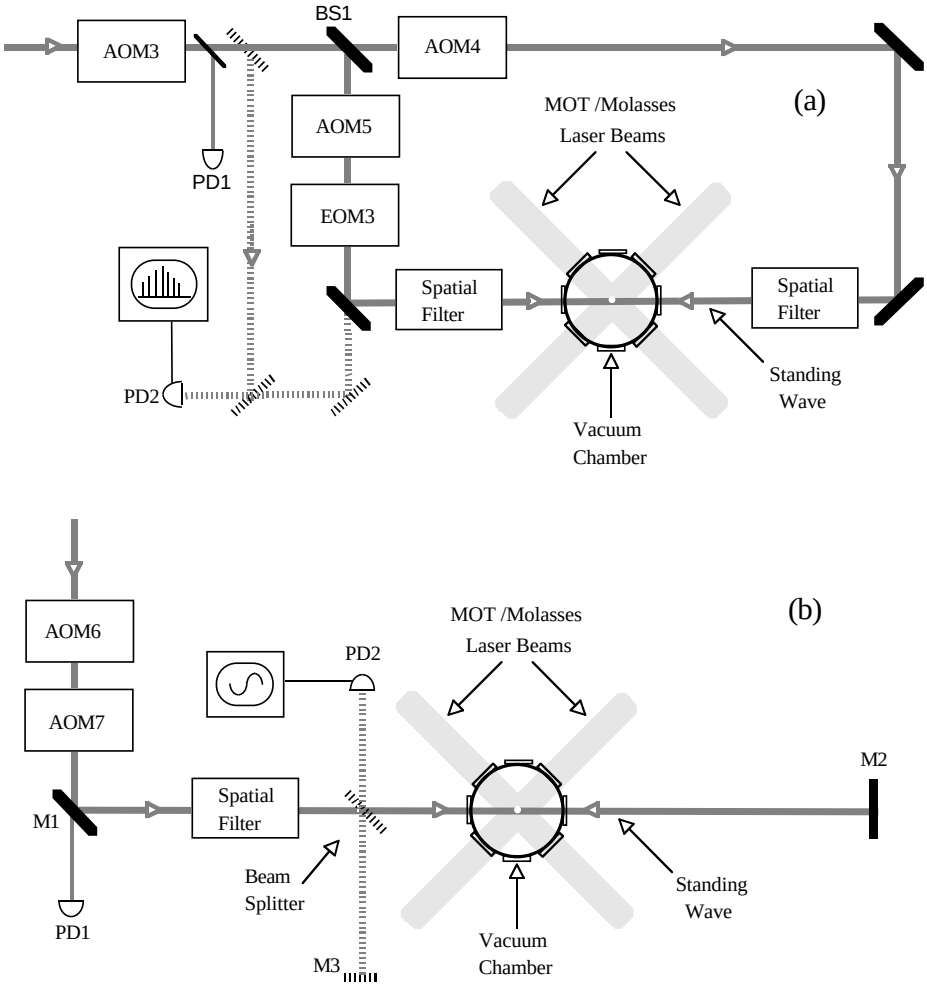

Figure 3.2: Beam configurations for the experiments. The MOT/molasses beams from Fig. 3.1 illuminate the atoms in the vacuum chamber in a standard $\sigma^+ - \sigma^-$ configuration, and the interaction beam is the source of the standing wave. For the experiment of Chapter 6, the standing wave was constructed of two counterpropagating beams with separate frequency shifts as depicted in part (a) of this figure. A differential shifting of the two beams provided the required control on the position (phase) of the standing wave. For the experiments of Chapters 4 and 5, the layout in (b) was used to provide the required control over the standing-wave amplitude.

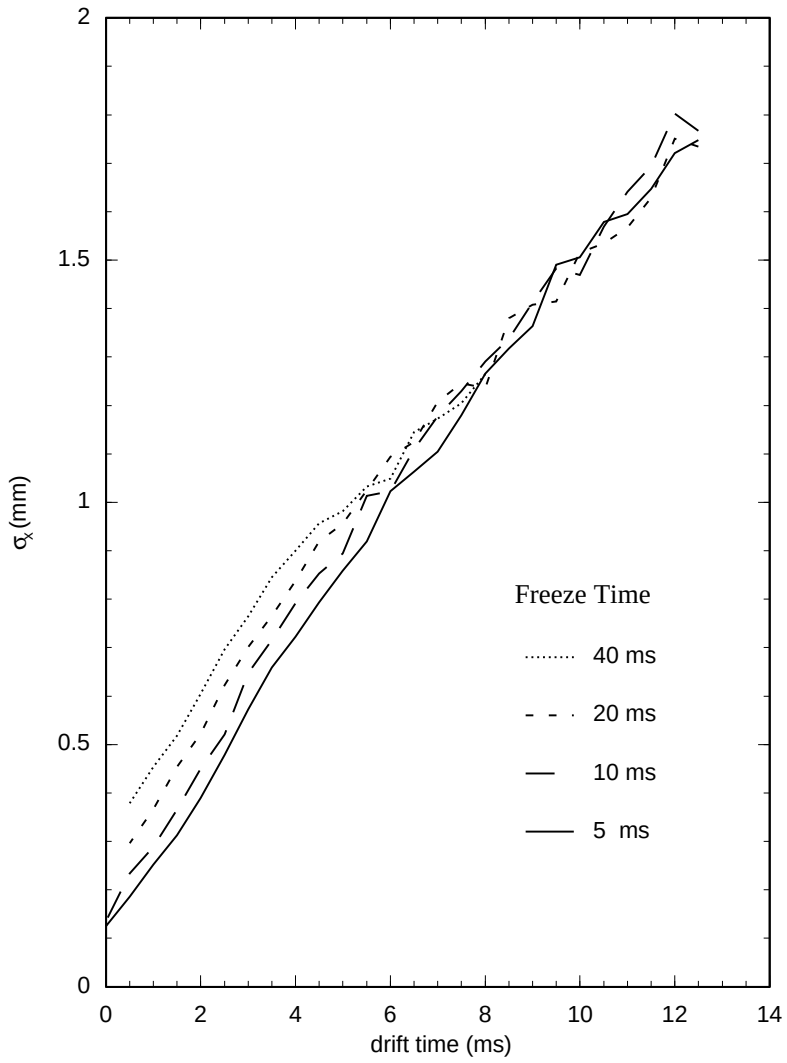

Figure 3.3: RMS spatial width as a function of free drift time. The constant slope of the curves for freeze times of 5 to 10 ms demonstrates the validity of this technique for measuring momentum. The RMS velocity of the distribution can be read from the slope of these curves. For longer freeze times there is significant atomic motion during the illumination by the molasses beams and the curves do not extrapolate to the initial condition. For this reason, the exposure on the camera was limited to 10 ms.

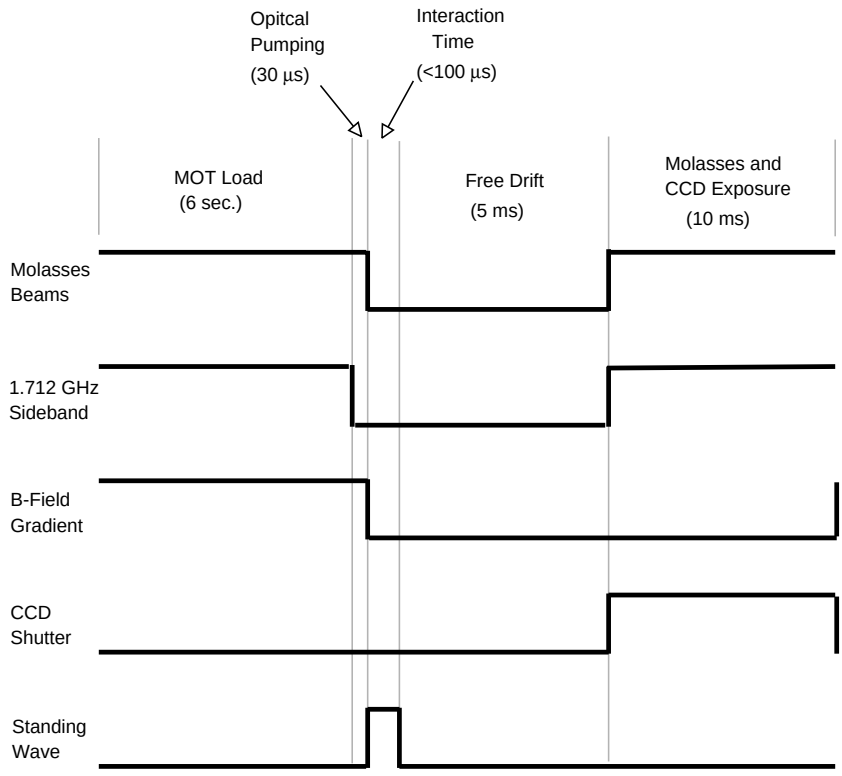

Figure 3.4: Timing diagram for various events in the experimental procedure. The initial loading of the magneto-optic trap is done with the atoms exposed to a magnetic field gradient and to cooling beams in the $\sigma^+ - \sigma^-$ configuration. Optical sidebands return the atoms to the cycling transition during the trapping, and are turned off shortly before the experiment to pump all the atoms into the $F = 1$ ground state. With the cooling and trapping fields turned off, the cold atoms are illuminated by the interaction beam, which forms a standing wave. The AC Stark shift from this standing wave provides a time-dependent potential which we control as described in the text. The signature of these interactions is a new atomic momentum distribution that translates into a spatial distribution after the period of free drift during which all the fields are turned off. The atomic sample is then frozen in optical molasses and imaged on a CCD camera. This record of the spatial distribution is then used to calculate the momentum distribution that resulted from the interaction.

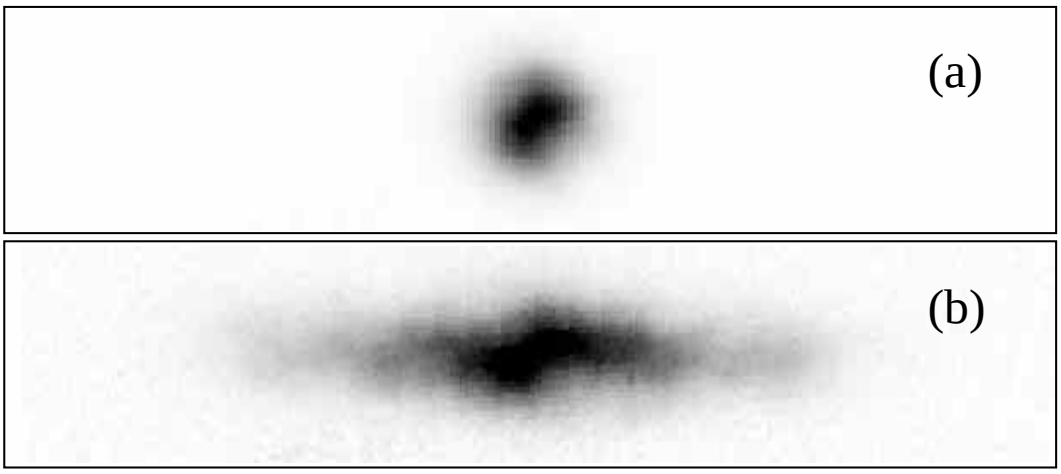

Figure 3.5: Two-dimensional atomic distributions after free expansion. (a) Initial thermal distribution with no interaction potential. (b) Dynamically localized distribution after interaction with the potential.

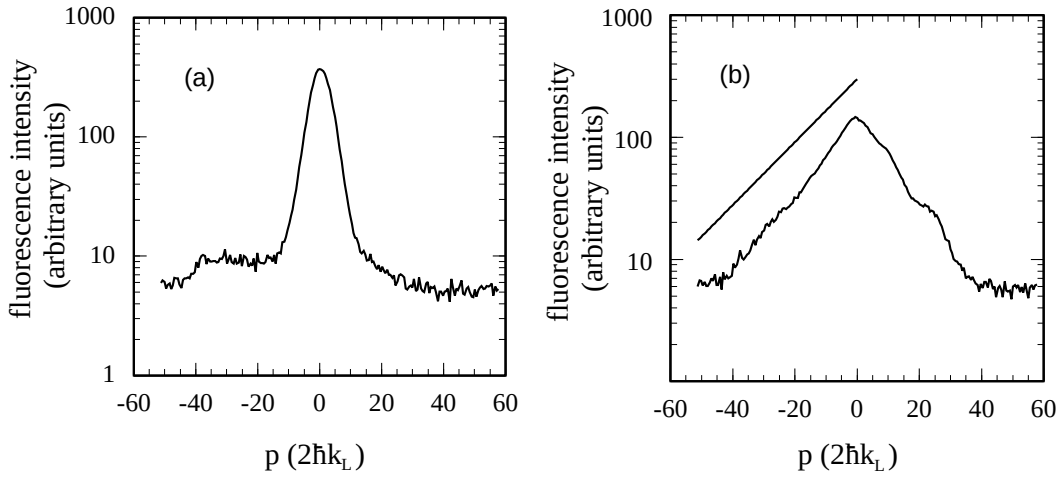

Figure 3.6: One-dimensional atomic momentum distributions. They were obtained by integrating along the vertical axes of the $2-D$ distributions in the previous figure. The horizontal axes are in units of two recoils, and the vertical axes show fluorescence intensity on a logarithmic scale. (a) Initial thermal distribution with no interaction. (b) Localized distribution after interaction with the potential. The significance of the characteristic exponential distribution is discussed in the text.

Chapter 4

Resonance Overlap in a Single-Pulse Interaction

4.1 Introduction

The simplest time-dependent potential is the turning on and off of an interaction, and one expects that for slow turn on/off the evolution will be adiabatic. The conditions for adiabatic behavior are usually very clear for linear potentials (the harmonic oscillator is an example) since there are only a few relevant time scales to consider. The difficulty with nonlinear potentials such as that occurring in the pendulum is that there are many time scales, so the conditions for adiabaticity must be examined much more carefully. The opposite extreme of fast passage is generally simpler to understand. We show that for time-scales intermediate to those of fast passage and adiabatic conditions, mixed phase space dynamics and chaos can be seen even with the mere act of turning an interaction on and off. In the context of atom optics, this type of time-dependent interaction is ubiquitous and occurs, for example, whenever an atomic beam passes through a standing wave of light.

The generic time-dependent Hamiltonian in this case is

$$H = \frac{p^2}{2M} + V_o f(t) \cos(2k_L x) \ . \tag{4.1}$$

A common form of the pulse is $f(t) = \exp[-(t/t_p)^2]$, which corresponds to an atomic beam traversing a Gaussian beam waist [25]. We consider here the case $f(t) = \sin^2(\pi t/T_s)$, where the interaction is turned on for a single period T_s.

This Hamiltonian can be expanded as

$$\begin{aligned} H &= \frac{p^2}{2M} + V_o \sin^2(\omega_m t/2)\cos(2k_L x) \\ &= \frac{p^2}{2M} + \frac{V_o}{2}\cos(2k_L x) \\ &\quad -\frac{V_o}{4}\cos(2k_L(x - v_m t)) - \frac{V_o}{4}\cos(2k_L(x + v_m t)) \ , \end{aligned} \tag{4.2}$$

where $\omega_m \equiv 2\pi/T_s$ is the angular frequency of the pulse, and $v_m \equiv \lambda_L/2T_s$. The effective interaction is that of a stationary wave with two counter-propagating waves moving at $\pm v_m$. The potential in this equation is composed of three terms, each having the form of a pendulum (Eq. 2.5), but with velocity offsets of $-v_m$, 0, and v_m. Classically, there are now three resonance zones each of width proportional to $\sqrt{V_o}$ and separation in momentum proportional to T_s^{-1}. A Poincaré surface of section for this Hamiltonian is shown in Fig. 4.1. Keeping V_o constant and increasing T_s leads to the overlap of these isolated resonances and the subsequent diffusion of the classical momentum distribution. This condition is the well known Chirikov resonance overlap criterion for global chaos in Hamiltonian systems [26, 27]. An example of a surface of section in that case is shown in Fig. 4.2. The parameters for resonance overlap are easily accessible experimentally [4].

4.2 Experimental Apparatus

To realize this system experimentally, we fixed the phase of the standing wave as described in Chapter 3 and Fig. 3.2(b). As in the delta-kicked rotor ex-

periments, AOM6 provided the control over the standing wave amplitude. To form the $\sin^2$ amplitude pulse, we utilized the response characteristics of the acousto-optic modulator. The first-order diffraction efficiency of an AOM is proportional to the square of the sine of the applied voltage, that is, the intensity of this diffracted light is $I = I_{max} \sin^2(\frac{\pi}{2} V/V_{sat})$, where V is the applied voltage and V_{sat} is the saturation voltage. The desired pulse shape can therefore be produced by a linear ramp up and down in the applied voltage.

4.3 The Resonance Overlap Criterion

To determine the resonance overlap criterion, we consider the widths of the three resonances in this system and their spacing from each other in phase space. There are three resonances in Eq. 4.2 that are centered (according to the stationary phase condition) at

$$\begin{aligned} \frac{p}{2\hbar k_L} &= 0 \ , \\ \text{and} \qquad \frac{p_\pm}{2\hbar k_L} &= \pm \frac{\omega_m}{8\omega_r} \ , \end{aligned} \tag{4.3}$$

with widths of

$$\begin{aligned} \frac{\Delta p_o}{2\hbar k_L} &= \sqrt{\frac{V_o}{\hbar \omega_r}} \ , \\ \text{and} \qquad \frac{\Delta p_\pm}{2\hbar k_L} &= \sqrt{\frac{V_o}{2\hbar \omega_r}} \ . \end{aligned} \tag{4.4}$$

If the islands are wide enough to meet the condition

$$\frac{\Delta p_o + \Delta p_\pm}{2} > \frac{2}{3} \ |p_\pm - p_o| \ , \tag{4.5}$$

then the neighboring resonances overlap [26, 27], and the particle can diffuse in phase space over a bounded region demarcated by Kolmogorov-Arnold-Moser

surfaces. This condition can be met experimentally by increasing the well depth with a fixed-pulse duration to broaden the resonances in Eq. 4.4. Alternatively, Eq. 4.3 indicates that the pulse duration can be increased with a fixed well depth to bring the resonances closer together.

The latter approach was used in our experiments for the practical consideration that it is generally more straightforward to lock the laser intensity and finely adjust the pulse duration than the converse. The critical pulse duration T_s^{cr} for the onset of resonance overlap can be estimated by combining Eqs. 4.4 and 4.5:

$$T_s^{cr} = \frac{2\sqrt{2}}{3(2+\sqrt{2})} \left(\frac{8\omega_r}{2\pi} \frac{V_o}{h} \right)^{-\frac{1}{2}} \ . \tag{4.6}$$

For durations T_s longer than this critical value, a particle exposed to the $\sin^2$ pulse can diffuse chaotically over an expanded region of phase space.

To experimentally determine the threshold $t_{p_{cr}}$ for overlap, we must distinguish between the momentum growth associated with spreading within the primary resonance and diffusion that can occur after resonance overlap. This distinction is accomplished by contrasting the momentum transfer from the $\sin^2$ pulse to the momentum transfer from a pulse of the same duration but with a constant amplitude

$$V'(x) = \frac{V_o}{2} \cos(2k_L x) \ . \tag{4.7}$$

This square-pulse interaction has a single resonance equivalent to the central resonance at $\rho_o = 0$ in the $\sin^2$ interaction,

$$V(x) = V'(x) - \frac{V_o}{4} \left[\cos(2k_L(x - v_m t)) + \cos(2k_L(x + v_m t)) \right] \ . \tag{4.8}$$

Under conditions that do not lead to resonance overlap, a sample of atoms that starts with an initial momentum of zero will be confined to the same region of

phase space in both of these interactions. The key to the interpretation of the experimental results is the realization that *for values of T_s below the threshold for resonance overlap $V'(x)$ and $V(x,t)$ should give the same result.* Under conditions that lead to resonance overlap, a larger region of phase space can be explored by the atoms exposed to the potential $V(x,t)$. For values of T_s greater than the overlap threshold, $V(x,t)$ will therefore result in significantly larger momentum transfer than $V'(x)$.

4.4 Experimental Results

The experimental results in Fig. 4.3(b) show the RMS momentum for both cases as a function of pulse duration (rise and fall times of 25 ns are included in the square-pulse duration). These measurements agree well with numerical classical simulations shown in Fig. 4.3(a), as well as with the estimated resonance overlap threshold [4].

How does the predicted quantum behavior compare with experiment and classical simulations? As seen from the dashed curve in Fig. 4.3(c), we find close agreement among all three for the square-pulse potential $V'(x)$. This result is interesting in its own right, since the coherent oscillations that occur for short times are seen in the experiment with a large ensemble of independent atoms as well as in the quantum simulation, which uses a single-wavepacket approach. For the case of $V(x,t)$ there is also good agreement among the three cases over the entire range of pulse times. However, the quantum widths are slightly lower than the corresponding classical values near the large peak in the RMS width. Although this difference is too small to be of quantitative significance, it is nevertheless the precursor for differences in quantum and classical behavior that

can occur when the classical dynamics are globally chaotic. These differences, which form the basis for the study of quantum chaos, are the focus of the next experiments we discuss.

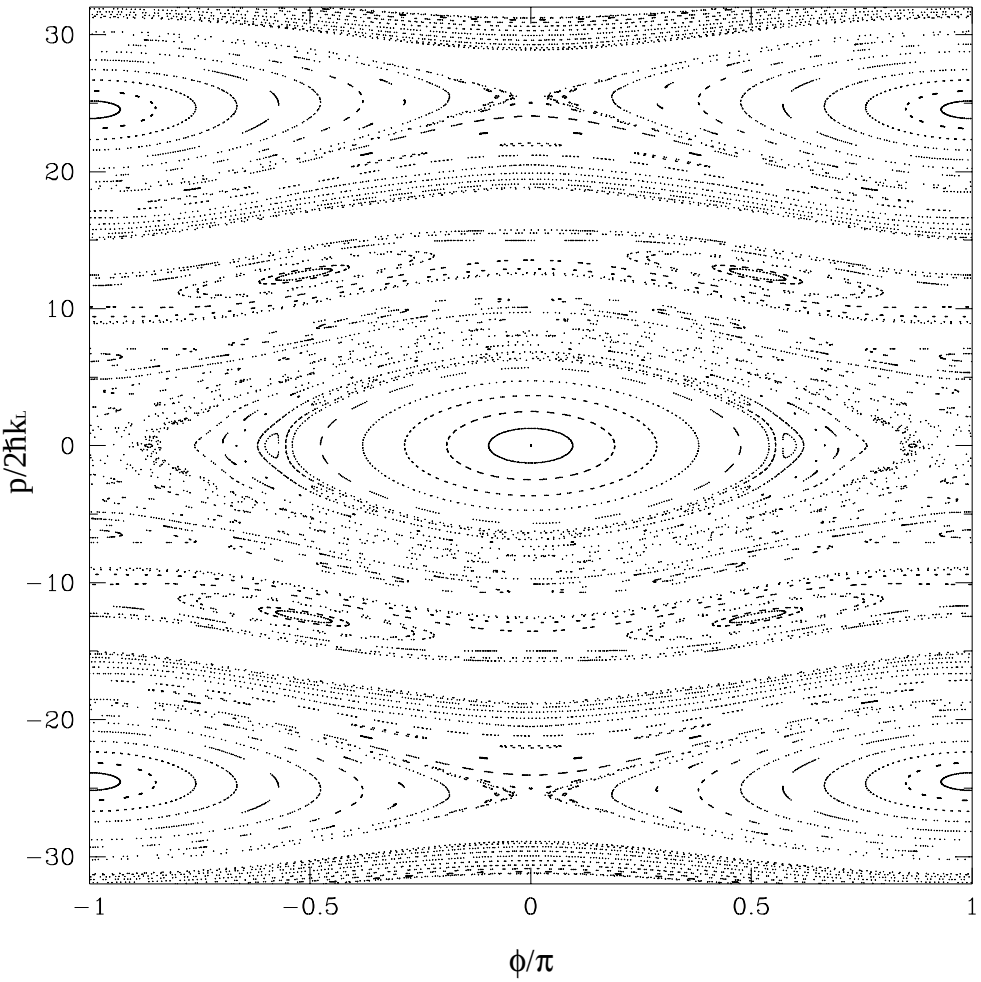

Figure 4.1: Poincaré surface of section for the $\sin^2$ potential. In this case there are three isolated resonances at $p/2\hbar k_L = 0$ and $\pm\, 25$.

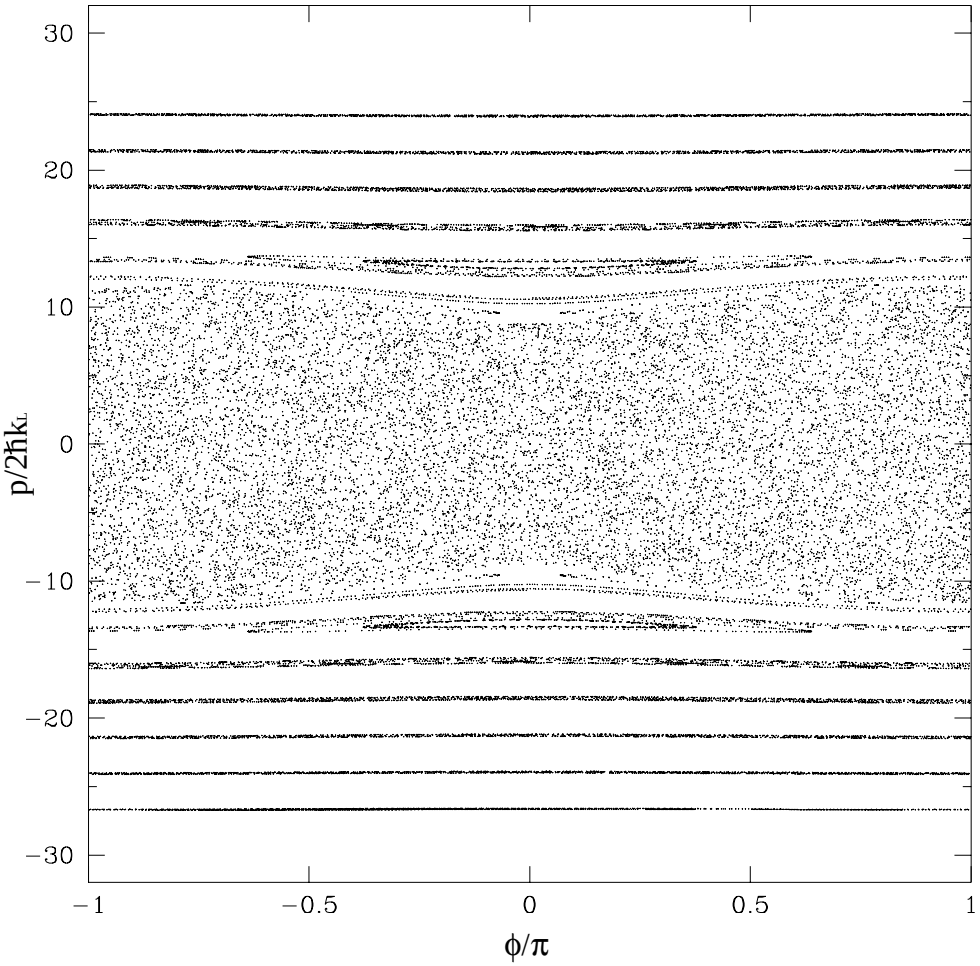

Figure 4.2: Poincaré surface of section for the $\sin^2$ interaction with a value of V_o leading to resonance overlap. In contrast with the previous figure, the system here has a bounded region of global chaos.

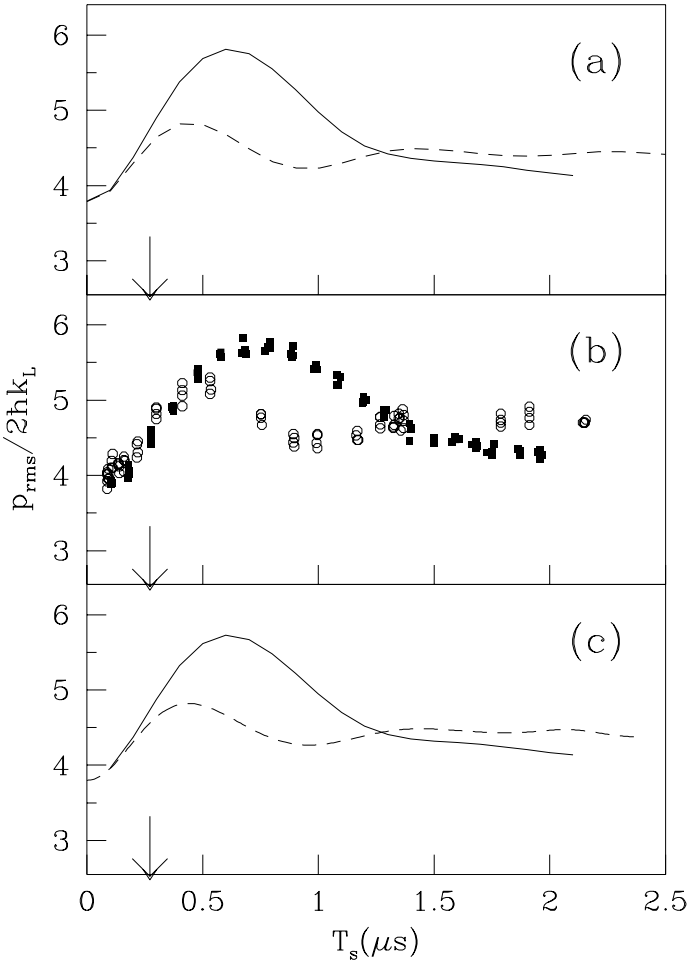

Figure 4.3: RMS momentum computed from (a) classical simulations for $\sin^2$ (solid line) and square (dashed line) pulses; (b) experimentally measured momentum distributions for $\sin^2$ (solid) and square (open) pulses; (c) corresponding quantum simulations. Here $V_o/h = 5.1$ MHz. The threshold estimated from resonance overlap is indicated by the arrow. A clear deviation occurs at a pulse duration close to the predicted value.

Chapter 5

The Kicked Rotor

5.1 Introduction

The classical delta-kicked rotor, or the equivalent standard mapping, is a textbook paradigm for Hamiltonian chaos [26, 19]. The Hamiltonian for the problem is given by

$$\mathcal{H} = \frac{\rho^2}{2} + K\cos\phi \sum_{n=-\infty}^{\infty} \delta(\tau - n) \ . \tag{5.1}$$

The evolution consists of resonant-kicks that are equally spaced in time, with free motion in between. The quantity K is called the stochasticity parameter, and is the standard control parameter for this system. As K is increased, the size of each resonant-kick grows. Beyond a threshold value of $K \approx 4$ it has been shown that phase space is globally chaotic [28]. The quantum version of this problem has played an equally important role for the field of quantum chaos, and a wide range of effects has been predicted [28]. In our realization, we have the cosine potential of the standing wave multiplied by a train of pulses with finite amplitude and pulse width. This system was analyzed previously in the context of molecular rotation excitation [29].

To achieve a system of the form in Eq. 5.1, we fixed the phase of our standing wave but turned its amplitude on and off in a series of N short pulses with period T. The optical arrangement was described in Chapter 3 (Fig. 3.2b).

The result was an interaction that can be described by the Hamiltonian of Eq. 2.7 with $F_{amp} = \sum_{n=1}^{N} F(t - nT)$ and $F_{ph} = 0$,

$$H = \frac{p^2}{2M} + V_o \cos(2k_L x) \sum_{n=1}^{N} F(t - nT) \ . \tag{5.2}$$

Here the function $F(t)$ is a narrow pulse in time centered at $t = 0$ that modulates the intensity of the standing wave. The sum in this equation represents the periodic pulsing of the standing wave amplitude by multiplying V_o with a value in the range $0 \leq F(t) \leq 1$.

The fast acousto-optic modulator (AOM6 in Fig. 3.2) provided the amplitude modulation of the standing wave to form the pulse train $\sum F(t)$. This modulator had a 10%-90% rise and fall time of 25 ns. To take advantage of the fast response of this modulator, its input signal was generated by a pulse generator with faster rise and fall times (4 ns). The computer that controlled the experiment downloaded the desired number of pulses and pulse period to a programmable arbitrary waveform generator, which in turn triggered the fast pulse generator.

A sample trace of the pulse profiles recorded on photodiode PD1 is shown in Fig. 5.1. The programmed profile had a constant amplitude, but because of signal limitations in the pulse generator and in AOM6, each pulse typically has a rounded but non-Gaussian profile. The consequences of this rounding are discussed below.

With the scaling introduced in Chapter 2 and the unit of time taken to be T, the period of our pulse train, the Hamiltonian for this system becomes

$$\mathcal{H} = \frac{\rho^2}{2} + K \cos\phi \sum_{n=1}^{N} f(\tau - n) \ . \tag{5.3}$$

The train of δ-functions in Eq. 5.1 has been replaced here by a series of normalized pulses $f(\tau) = F(\tau T)/\int_{-\infty}^{\infty} F(\tau T)d\tau$. Note that the scaled variable $\tau = t/T$ measures time in units of the pulse period. As described earlier, $\phi = 2k_L x$ is a measure of an atom's displacement along the standing wave axis and ρ is its momentum in units of $2\hbar k_L/\hbar$.

An ideal realization of the delta-kicked rotor would have pulses of infinite amplitude and infinitesimal duration. Obviously this limit is beyond a practical realization, but (as discussed below) if the atoms do not move significantly during a pulse, the finite-pulse system is an excellent approximation of the delta-kicked rotor. Aside from the temporal profile of the pulses, all the experimental parameters that determine the classical evolution of this system are combined into one quantity, the stochasticity parameter K. As we will see, the quantum evolution depends additionally on the parameter $\bar{k}$. These two dimensionless quantities thus characterize the dynamics of Eq. 5.3. In terms of the physical parameters of Eq. 5.2, they are

$$K \equiv 8V_o\alpha T t_p \omega_r/\hbar \tag{5.4}$$

$$\bar{k} = 8\omega_r T \ . \tag{5.5}$$

Here t_p is the FWHM duration of each pulse, and $\alpha \equiv \int_{-\infty}^{\infty} F(t)dt/t_p$ is a shape factor that characterizes the integrated power for a particular pulse profile: it is the ratio of the energy in a single pulse to the energy of a square pulse with the same amplitude and duration. For a train of square pulses, $\alpha = 1$; for Gaussian pulses, $\alpha = (\pi/4\ln 2)^{1/2} = 1.06$. For the roughly square pulses realized in our experiments, α was within a few percent of unity.

5.2 Classical Predictions and Consequences of the Finite Pulse Duration

Atoms with low velocities do not move significantly during the pulse, so their classical motion can be described by a map. By integrating Hamilton's equations of motion over one period, we obtain the change in an atom's displacement and momentum:

$$\begin{aligned} \Delta\phi &= \int_{n-\frac{1}{2}}^{n+\frac{1}{2}} dt\ \rho = \rho \\ \Delta\rho &= \int_{n-\frac{1}{2}}^{n+\frac{1}{2}} dt\ K\sin\phi \sum f(\tau - n) = K\sin\phi\ . \end{aligned} \tag{5.6}$$

The discretization of these relations is the classical map,

$$\begin{aligned} \phi_{n+1} &= \phi_n + \rho_{n+1} \\ \rho_{n+1} &= \rho_n + K\sin\phi_n\ , \end{aligned} \tag{5.7}$$

that is known as the Taylor-Chirikov or "standard" map [28, 30]. For small values of K, the phase space of this extensively studied system shows bounded motion with regions of local chaos. Global stochasticity occurs for values of K greater than ~ 1, and widespread chaos appears at $K >\sim 4$, leading to unbounded motion in phase space [31]. Correlations between kicks in the spatial variable ϕ can be ignored for large values of K, so this map can be iterated to estimate the diffusion constant. After N kicks, the expected growth in the square of the momentum is

$$\langle(\rho_N - \rho_0)^2\rangle = K^2 \sum_{n=0}^{N-1} \langle \sin\phi_n^2\rangle + K^2 \sum_{n\neq n'}^{N-1} \langle \sin\phi_n \sin\phi_{n'}\rangle \tag{5.8}$$

$$= \frac{K^2}{2} N\ . \tag{5.9}$$

The diffusion in momentum is thus

$$\langle \rho^2 \rangle = DN, \quad \text{with } D \equiv \frac{K^2}{2}. \tag{5.10}$$

Note that this description, which follows from the discretization into the standard map, requires the duration of the pulses to be short. To understand the effects of a finite pulse-width, consider the case where the pulse profile $f(\tau)$ is Gaussian with an RMS width τ_{RMS}. In the limit of a large number of kicks N, the potential in Eq. 5.3 can be expanded into a Fourier series:

$$\begin{aligned} \mathcal{H} &= \frac{\rho^2}{2} + K \cos\phi \sum_{m=-\infty}^{\infty} e^{im2\pi\tau} e^{-(m2\pi\tau_{\text{RMS}})^2/2} \\ &= \frac{\rho^2}{2} + \sum_{m=-\infty}^{\infty} K_m \cos(\phi - m2\pi\tau) \end{aligned} \tag{5.11}$$

with

$$K_m \equiv K \ \exp\left[-(m2\pi\tau_{\text{RMS}})^2/2\right] \ . \tag{5.12}$$

The nonlinear resonances are located (according to the stationary phase condition) at $\rho = d\phi/d\tau = m2\pi$. This expansion is similar to the resonance structure of the delta-kicked rotor, in which the K_m are constant for all values of m. In Eq. 5.11, however, the widths of successive resonances fall off here because of the exponential term in the effective stochasticity parameter K_m. This fall-off is governed by the pulse profile; the result of Eq. 5.11 was derived particularly for a Gaussian pulse shape, but in general K_m is given by the Fourier coefficients of the periodic pulse train.

The nonzero pulse widths thus lead to a finite number of significant resonances in the classical dynamics, which in turn limits the diffusion that results from overlapping resonances to a band in momentum. However, by

decreasing the pulse duration and increasing the well depth, the width of this band can be made arbitrarily large, approaching the δ-function pulse result. This can be seen in the result derived above. In the limiting case of $\tau_{\mathrm{RMS}} \to 0$ with K fixed (infinitesimal pulse width and large well depth), we recover the resonance structure expected for the δ-function limit in Eq. 5.1: $K_m = K$. In practice however, it is not necessary to have an infinitesimal pulse width. To model the delta-kicked rotor, the pulse width only needs to be small enough that the band of diffusion is significantly wider than the range of atomic momenta in the experiment and that the effective diffusion constant K_m is approximately uniform over this range.

An example of the bounded region of chaos that arises from the finite pulse duration is illustrated by the classical phase portrait shown in Fig. 5.2, for typical experimental parameters. The central region of momentum in this phase portrait is in very close correspondence with the delta-kicked rotor model with $K = 11.6$. This stochasticity parameter is well beyond the threshold for global chaos.

The boundary in momentum can also be understood using the concept of an impulse. If the atomic motion is negligible while the pulse is on, the momentum transfer occurs as an impulse, changing the momentum of the atom without significantly affecting its position. Atoms with a sufficiently large velocity, however, can move over several periods of the potential while the pulse is on. The impulse for these fast atoms is thus averaged to zero, and acceleration to larger velocities is inhibited. The result is a momentum boundary that can be pushed out by making each pulse shorter.

Classically, then, the atoms are expected to diffuse in momentum until

they reach the momentum boundary that results from the finite pulse width. Equation 5.10 indicates that the energy of the system $\langle \frac{1}{2}(p/2\hbar k_L)^2 \rangle$ thus grows linearly in time. In terms of the number of pulses N, this energy is

$$\left\langle \frac{1}{2}\left(\frac{p}{2\hbar k_L}\right)^2 \right\rangle = \left\langle \frac{1}{2}\left(\frac{\rho}{\bar{k}}\right)^2 \right\rangle = \frac{1}{2\bar{k}^2}\frac{K^2}{2}N \ . \tag{5.13}$$

The delta-kicked rotor is an especially important system in the study of quantum chaos because the classical analog has been so well studied and because its time-evolution operator can be found analytically [28].

5.3 Quantum Predictions

This system can be expected to show quantum behaviors that are very different from those predicted by classical analyses. Indeed, the kicked rotor bears a striking resemblance to the physical model of a particle passing through a series of diffraction gratings, which is intrinsically quantum mechanical. In the diffraction problem, a particle undergoes intervals of free flight that are interrupted by short periods of interaction with a grating. During these interactions its transverse motion is modified by a periodic potential; this modification can lead to interference between the set of possible paths through the gratings. The properties of the resulting interferometer depend on the periodic structure of the gratings and time of flight between successive gratings. Likewise, in the kicked-rotor a particle is repeatedly subjected to brief periodic potentials, between which it undergoes free evolution. The structure of the sinusoidal potential is given by its amplitude K, and the kicking period T is characterized by the dimensionless parameter $\bar{k} \equiv 8\omega_r T$. As in the case of an interferometer constructed from a series of diffraction gratings, the kicked rotor has important

features that require a quantum description. We discuss here two of these features, dynamical localization and quantum resonances. Dynamical localization is the quantum suppression of chaotic diffusion, which can be modeled in various systems but is most cleanly studied in the delta-kicked rotor. Quantum resonances are a quantum feature particular to the delta-kicked rotor.

A quantum analysis of this system starts with the Schrödinger equation, Eq. 2.12. For the pulsed modulation of Eq. 5.3, this becomes

$$i\bar{k}\frac{\partial}{\partial\tau}\Psi(\phi,\tau) = \left[\frac{-\bar{k}^2}{2}\frac{\partial^2}{\partial\phi^2} + K\cos\phi\sum_n f(\tau-n)\right]\Psi(\phi,\tau)\ . \tag{5.14}$$

The periodic time dependence of the potential implies that the orthogonal solutions to this equation are time-dependent Floquet states. This system has been studied extensively in the ideal case of $f(\tau) = \delta(\tau)$ with an infinite train of kicks ($n = 0, \pm1, \pm2, ...$) [32]. An analysis of this system by Chirikov, Izrailev, and Shepelyansky [33] shows that this system diffuses classically only for short times during which the discrete nature of the Floquet states is not resolved. As shown in Ref. [28], Eq. 5.14 can be transformed into the form of the tight-binding model of condensed-matter physics. An analysis of that system indicates that the Floquet states of Eq. 5.14 are discrete and exponentially localized in momentum. Since these states form a complete basis for the system, the initial condition of an atom in the experiments can be expanded in a basis of Floquet states. Subsequent diffusion is limited to values of momentum covered by those Floquet states that overlap with the initial conditions of the experiment. If the initial conditions are significantly narrow in momentum, the energy of the system should grow linearly with the number of kicks N, in agreement with the classical prediction in Eq. 5.13, until a "quantum break

time" N^*. After this time, the momentum distribution approaches that of the Floquet states that constituted the initial conditions, and the linear growth of energy is curtailed. This phenomenon is known as dynamical localization.

The Floquet states are typically localized with an exponential distribution in momentum. They are characterized by a "localization length" ξ with $|\Psi(\rho/\hbar)|^2 \sim \exp(-|\rho/\hbar|/\xi)$. The momentum distribution then has a $1/e$ half-width given by $p^*/2\hbar k_L = \rho^*/\hbar \equiv \bar{\xi}$, where $\bar{\xi}$ is the average localization length of the Floquet states [28, 34]. The number of Floquet states that overlap the initial condition (and therefore the number of Floquet states in the final state) is roughly $\bar{\xi}$, so the average energy spacing between states is $\Delta\omega \sim 1/\bar{\xi}$. The quantum break time is the point after which the evolution reflects the discreteness of the energy spectrum, hence $N^* \Delta\omega \sim 1$, or $N^* = \bar{\xi}$. By combining these estimates with Eq. 5.13, we see that $\bar{\xi}$ is proportional to $K^2/2\hbar^2$. The constant of proportionality has been determined numerically to be $\frac{1}{2}$ [34], and the localization length is thus

$$\frac{p^*}{2\hbar k_L} = \bar{\xi} = \frac{K^2}{4\hbar^2}. \tag{5.15}$$

In our experiments it is the RMS momentum that is recorded, since its definition applies as well to the pre-localized Gaussian distributions as to the exponentially localized ones. For an exponential distribution, this quantity is larger than the localization length by a factor of $\sqrt{2}$:

$$\frac{p^*_{\mathrm{RMS}}}{2\hbar k_L} = \sqrt{2}\frac{p^*}{2\hbar k_L} = \frac{K^2}{2\sqrt{2}\hbar^2} \tag{5.16}$$

Since $\bar{\xi}$ is also a measure of the number of kicks before diffusion is limited by dynamical localization, we have for the quantum break time

$$N^* = \bar{\xi} = \frac{K^2}{4\hbar^2}. \tag{5.17}$$

An inherent assumption in the derivation of Eqs. 5.15-5.16 is the lack of structure in the phase space of the system. Small vestigial islands of stability, however, do persist even for values of K greater than 4. This structure introduces in the dynamics a dependence on the the location of the initial conditions in phase space. Nonetheless, this analysis provides a useful estimate of the localization length and the quantum break time.

5.4 Experimental Parameters

It is important to consider these last two relations in choosing experimental parameters. In order for a localized distribution to be observable, p^* must be significantly smaller than the region enclosed by the classical boundary to diffusion. Thus there is a constraint between the duration of the kicks (parameterized by its FWHM value t_p) and the localization length. As described above, the simplest estimate for this condition requires that the distance traveled by a particle during a pulse be much less than a period of the standing wave: $p^*_{\text{RMS}} t_p/M << \lambda_L/2$. A better estimate comes from Eq. 5.12, which indicates the effective stochasticity parameter for a particle with momentum $p/2\hbar k_L = m2\pi/\hbar$ in a train of Gaussian pulses with FWHM duration $t_p = \sqrt{8\ln 2}\,\tau_{\text{RMS}} T$. From this equation we see that the effective stochasticity parameter drops below 4, resulting in islands of stability for atoms with momenta greater than $p_{max}/2\hbar k_L = (\ln 2 \ln \frac{K}{4})^{\frac{1}{2}}/2\omega_r t_p$. The resonance overlap criterion can provide a more accurate expression, but this estimate is sufficient for determining the range of operating parameters. The experimental conditions should be chosen so that the localized momentum width p^*_{RMS} is much smaller than this limit. On the other hand, the localized momentum distribu-

tion needs to be several times wider than the initial distribution so that it can be distinguished from the initial conditions. The atoms in our MOT started with an RMS momentum of $\sigma_{po} = \sim 4.6\,\hbar k_L$, imposing a lower limit on the localization length of $p^*_{\rm RMS}/2\,\hbar k_L > \sigma_{po}/2\,\hbar k_L = 2.3$. Combining these two bounds gives,

$$\frac{\sigma_{po}}{2\,\hbar k_L} < \frac{p^*_{\rm RMS}}{2\,\hbar k_L} < \frac{\sqrt{\ln 2 \ln \frac{K}{4}}}{2\omega_r t_p} \ . \tag{5.18}$$

Another constraint on the localization length comes from its relation to N^*, the number of kicks required for the localization to manifest. This time must be short enough to be observable in the experiment. Indeed, the experiment should continue for a time significantly greater than N^* so that it is clear that the early period of diffusive growth has ended. An upper limit on the duration of the experiment, and therefore on the localization length, comes from the increased probability of spontaneous emission events with longer exposures to the standing wave. Spontaneous emission can randomize the phase of an atomic wavefunction, thereby destroying the coherence necessary for the quantum phenomena under observation. The probability of a spontaneous event during N^* kicks of duration t_p is $1 - e^{-\gamma_{spont} N^* t_p}$. To preserve the coherent evolution of the atomic sample, we require this probability to be small:

$$\gamma_{spont} N^* t_p << 1 \ . \tag{5.19}$$

Here $\gamma_{spont} = (V_o \delta_L/\hbar)(\Gamma/2)[\delta_L^2 + (\Gamma/2)^2]^{-1}$ is the probability per unit time for an atom to undergo a spontaneous event, and $\Gamma/2\pi$ (= 10 MHz) is the linewidth of the sodium D_2 transition.

In addition to these constraints relating to the localization length, there are several other restrictions on the experimental parameters. To ensure that

the atoms are all subject to the same well depth, the light field cannot vary greatly over the sample of atoms, and thus a lower limit to the beam waist is given by the spatial width of the atomic sample. In our experiments the interaction times were short enough and the initial temperatures cold enough that the sample of atoms did not spread significantly from its initial MOT width of $\sigma_{xo} \sim 0.15$ mm (RMS), so it was sufficient for the beam waists to be large in comparison to this initial value,

$$w_o >> \sigma_{xo} \ . \tag{5.20}$$

In order to observe dynamical localization, the classical phase space must be characterized by extended regions of chaos evident in the classical phase portraits for values of the stochasticity parameter greater than 4. The experiment needs to be a realization of the kicked rotor in this regime,

$$K > 4 \ . \tag{5.21}$$

According to Eq. 5.4, this constraint introduces a relationship among the well-depth V_o, the pulse period T, and the pulse duration t_p.

The most important constraint on the experimental realization of this system is the maximum power available in the beams that make up the standing wave. In fact, the greater this available power, the less restrictive most of the previous constraints become. For example, with unlimited laser power, Eqs. 5.18 and 5.19 can be satisfied by making t_p sufficiently small, and the well depth can be increased as necessary to satisfy this last constraint ($K > 4$). Large laser powers also help satisfy Eq. 5.20, since the beams can then be made wide while maintaining the desired irradiance at the center of the beam profile. In

practice, however, the laser power in each beam (P) is of course limited and the other experimental control parameters of beam waist (w_o), detuning (δ_L), pulse period (T), and pulse duration (t_p) must all be chosen to satisfy the criteria enumerated here.

The fact that Eq. 5.19 can be satisfied is an especially valuable aspect of this experiment. Spontaneous emission is the only significant avenue of energy dissipation from the dilute sample of atoms. By making this dissipation negligible, we effectively realize a conservative Hamiltonian system. It is interesting to note the features of the system that make this realization possible. To keep the probability of spontaneous emission small, we take advantage of the different dependencies of the well depth V_o and the spontaneous emission rate γ_{spont} on the detuning. The well depth is a relatively soft function of the detuning; according to Eq. 2.6 it is proportional to the intensity of the standing wave and inversely proportional to the detuning,

$$\begin{aligned} V_o &= \frac{2}{3}\frac{\hbar(\Gamma/2)^2}{\delta_L}\frac{I}{I_{sat}} \\ &\propto \frac{\mathrm{P}}{w_o^2\,\delta_L}\,. \end{aligned} \tag{5.22}$$

Although the spontaneous emission rate is also proportional to the intensity, it varies as the inverse square of the detuning,

$$\begin{aligned} \gamma_{spont} &= \frac{V_o\delta_L}{\hbar}\,\frac{\Gamma/2}{\delta_L^2+(\Gamma/2)^2} \\ &\simeq \frac{V_o}{\delta_L}\,\frac{\Gamma/2}{\hbar} \\ &\propto \frac{\mathrm{P}}{w_o^2\,\delta_L^2}\,. \end{aligned} \tag{5.23}$$

Within the limits of available laser power, a large detuning can therefore provide

negligible spontaneous emission during the experiment without too much loss in the well depth.

Having a large detuning also satisfies one of the approximations in the derivation of Eq. 5.2, that is, that the detuning δ_L needs to be large in comparison with the linewidth and recoil frequency of the sodium D_2 transition. The detuning also needs to be larger than the spacing between the $F=1$ and $F=2$ sublevels of the ground state (1.7 GHz) to minimize the effects of incomplete optical pumping. These conditions were well satisfied by the more stringent detunings needed to make the probability of spontaneous emission small.

A maximum limit on the detuning comes from the need to avoid exciting other transitions that would affect the calculation of the well depth V_o. The nearest competing transition in our system was the sodium D_1 line, approximately 500 GHz to the red of the D_2 transition.

To sort through the various requirements and limitations on the multidimensional space of the experimental control parameters, we created spreadsheets that listed ranges of the parameters and displayed the relevant quantities that resulted from them. We then identified combinations of the various control parameters that satisfied the above criteria and were accessible to our experimental set-up.

Typically, each counter-propagating beam had a power of $P = 0.2 - 0.4$ W; the waists were in the range of $w_o = 1.2 - 2.2$ mm, and the detunings from resonance $\delta_L/2\pi$ were between 5 and 10 GHz. These operating conditions led to well depths in the range of $V_o/h = 5 - 15$ MHz, and to spontaneous emission probabilities of about 1% per kick. The pulse periods and durations

were in the ranges $1-5$ μs and $0.05-0.15$ μs, respectively.

5.5 Experimental Results

We subjected the cooled and trapped atoms to the periodically pulsed standing wave of Eq. 5.2 and recorded the resulting momentum distributions as described in Chapter 3. To study the temporal evolution of the atomic sample under the influence of the periodic kicks, these experiments were repeated with increasing numbers of kicks (N) with the well depth, pulse period, and pulse duration fixed. These successive measurements provided the momentum distributions at different times in the atomic sample's evolution. Such a series of measurements is shown in Fig. 5.3. Here the pulse had a period of $T = 1.58$ μs, and a FWHM duration of $t_p = 100$ ns. For these conditions, $\bar{k}$ has a value of 2.0. The largest uncertainty in the experimental conditions is in the well depth, V_o, which depends on the measurement of the absolute power of the laser beams that make up the standing wave and their spatial profile over the sample of atoms. To within 10%, the well-depth for these data had spatial RMS value of $V_o/h = 9.45$ MHz. The pulse profile was nearly square, leading to a stochasticity parameter of $K = 11.6$, the same value as for the phase portrait in Fig. 5.2.

The distributions clearly evolve from an initial Gaussian at $N = 0$ to an exponentially localized distribution after approximately $N = 8$ kicks. We have measured distributions out until $N = 50$ and find no further significant change. The small peak on the right side of this graph is due to nonuniformities in the detection efficiency. As discussed in Chapter 3, the relative numbers of atoms with different momenta is measured by their fluorescence intensity on a CCD camera. Factors such as spatial variations in the illuminating light and

unevenness in the chamber windows between the atomic sample and the CCD camera lead to minor limitations like this on the resolution of the momentum measurements.

The growth of the mean kinetic energy of the atoms as a function of the number of kicks was calculated from the data and is displayed in Fig. 5.4. It shows an initial diffusive growth until the quantum break time $N^* = 8.4$ kicks, after which dynamical localization is observed [3]. The solid line in this figure represents the classical diffusion predicted in Eq. 5.13. The data follow this prediction until the break time. The dashed line in the same figure is the prediction for the energy of the localized distribution from Eq. 5.16. Though not shown here, classical and quantum calculations both agree with the data over the diffusive regime. After the quantum break time, the classical growth slows slightly due to the fall-off in K predicted by Eq. 5.12 for non-stationary atoms. The observed distribution would lead to a reduction of only 15% in the stochasticity parameter. Thus, the classically predicted energy would continue to increase diffusively. The measured distributions, however, stop growing as predicted by the quantum analysis.

The deviations in the data of Fig. 5.4 from the predicted values underline some of the limitations in the derivations of the diffusion constant (Eq. 5.10) and localization length (Eq. 5.15) of the delta-kicked rotor. The classical and quantum derivations that led to these analytic results assumed that the phase space of the system had no underlying structure, that is, that there were no correlations in the motion between successive kicks. This assumption is strictly true only in the limit of infinite K [35]. For finite values of the stochasticity parameter, these expressions cannot be considered exact values since the true

dynamics would have some dependence on the location of the initial conditions in phase space. They do, however, provide useful estimates for the diffusion rate and localization length of the delta-kicked rotor. Indeed, an important feature of the delta-kicked rotor is that these estimates can be adapted to other systems whose dynamics are characterized locally by overlapping resonances.

This experimental realization of the delta-kicked rotor is significant for its striking demonstration of a departure from the classical prediction of continued diffusion. In addition to this information about the system's energy, the experiment provides a picture of the entire momentum distribution. The observed exponentially localized distributions are the hallmark of dynamical localization. These experimental results are in good absolute agreement with theoretical predictions, and this agreement is obtained without the fitting of any adjustable parameters. These results are the first experimental observation of the onset of dynamical localization in time, and of the quantum break time [3].

5.6 Quantum Resonances

Between kicks, the atoms undergo free evolution for a fixed duration. The quantum phase accumulated during the free evolution is $e^{-ip^2T/2M\hbar}$. An initial plane wave at $p = 0$ couples to a ladder of states separated by $2\hbar k_L$. For particular pulse periods, the quantum phase for each state in the ladder is a multiple of 2π, a condition known as a "quantum resonance" [28]. More generally, a quantum resonance is predicted when the accumulated phase between kicks is a rational multiple of 2π. We have scanned T from 3.3 μs to 50 μs and find quantum resonances when the quantum phase is an integer multiple of π

. For even multiples, the free evolution factor between kicks is unity; for odd multiples, there is a flipping of sign between each kick. Quantum resonances have been studied theoretically, and it was shown that instead of localization, one expects the energy to grow quadratically with time [36]. This picture, however, is only true for an initial plane wave. A general analysis of the quantum resonances shows that for an initial Gaussian wavepacket, or for narrow distributions not centered at $p = 0$, the final momentum distribution is actually smaller than the exponentially localized one, and settles in after a few kicks [37]. Our experimental results are shown in Fig. 5.5. Ten quantum resonances are found for T ranging between 5 μs (corresponding to a phase shift of π) and 50 μs (10π) in steps of 5 μs. The saturated momentum distribution as a function of T are shown in Fig. 5.5(a). The narrower, non-exponential profiles are the resonances between which the exponentially localized profiles are recovered. The time evolution of the distribution at a particular resonance is shown in Fig. 5.5(b), from which it is clear that the distribution saturates after very few kicks.

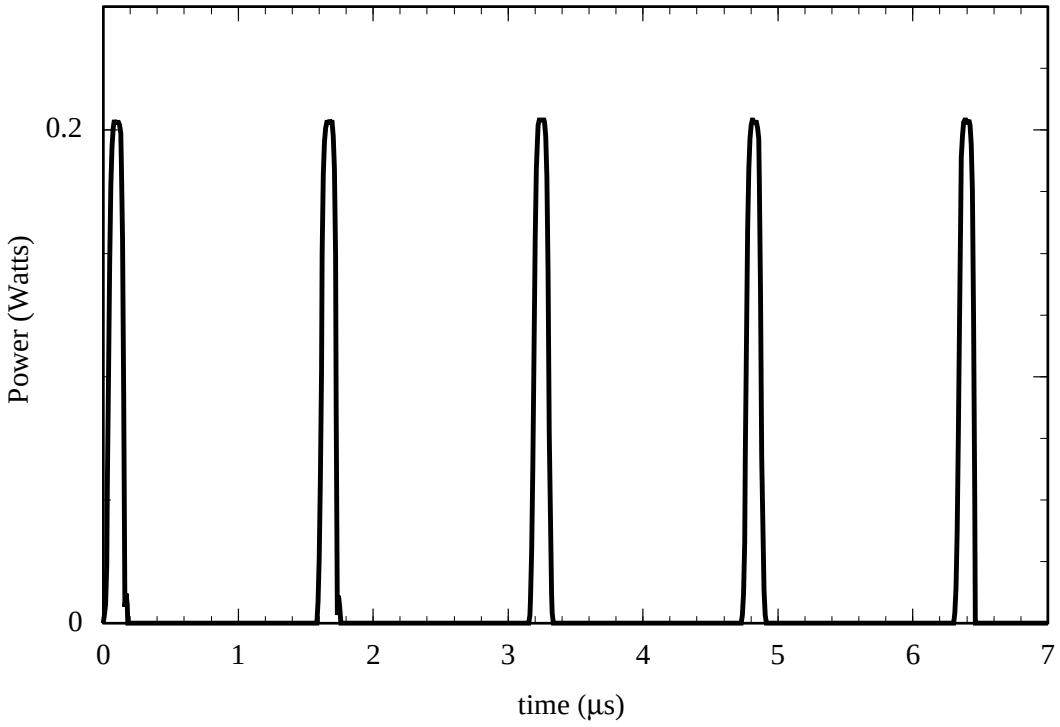

Figure 5.1: Digitized temporal profile of the pulse train as measured on a fast photodiode. The vertical axis represents the power in one beams of the standing wave. The pulse profile $f(t)$ and the well depth V_o are derived from this scan.

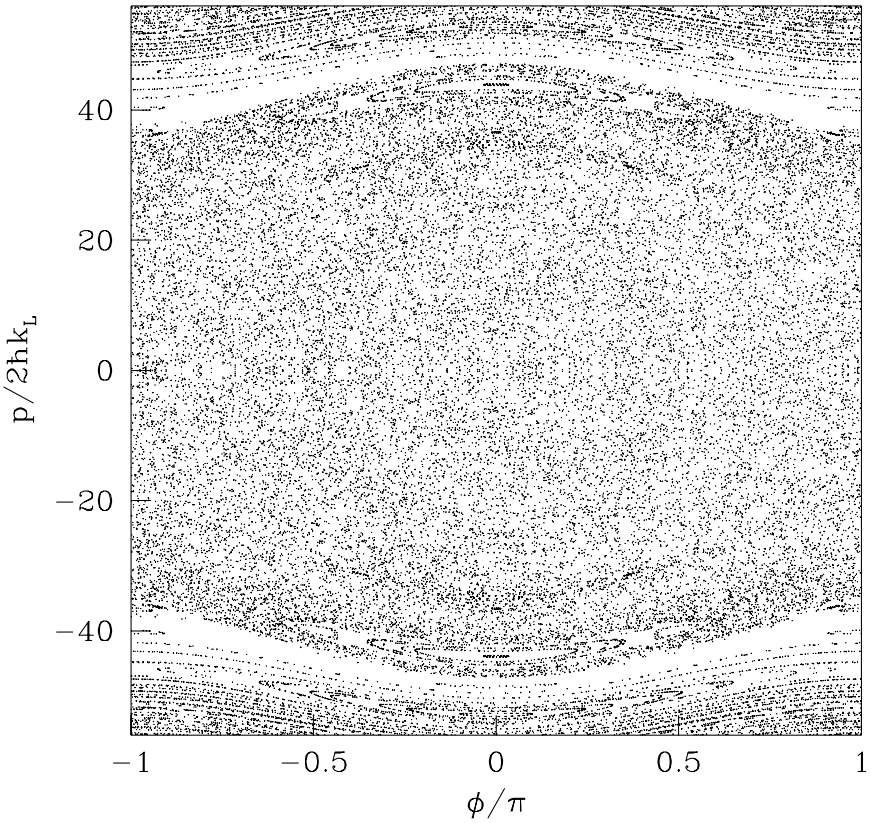

Figure 5.2: Poincaré surface of section for the kicked rotor using a train of Gaussian pulses of width $t_p/T = 1/15.8$ (FWHM) to simulate the experimental sequence. The stochasticity parameter in this calculation is $K = 11.6$. The central region of the portrait shows the chaotic motion expected for this value of the stochasticity parameter. Bounding regions due to the finite pulse width are also evident.

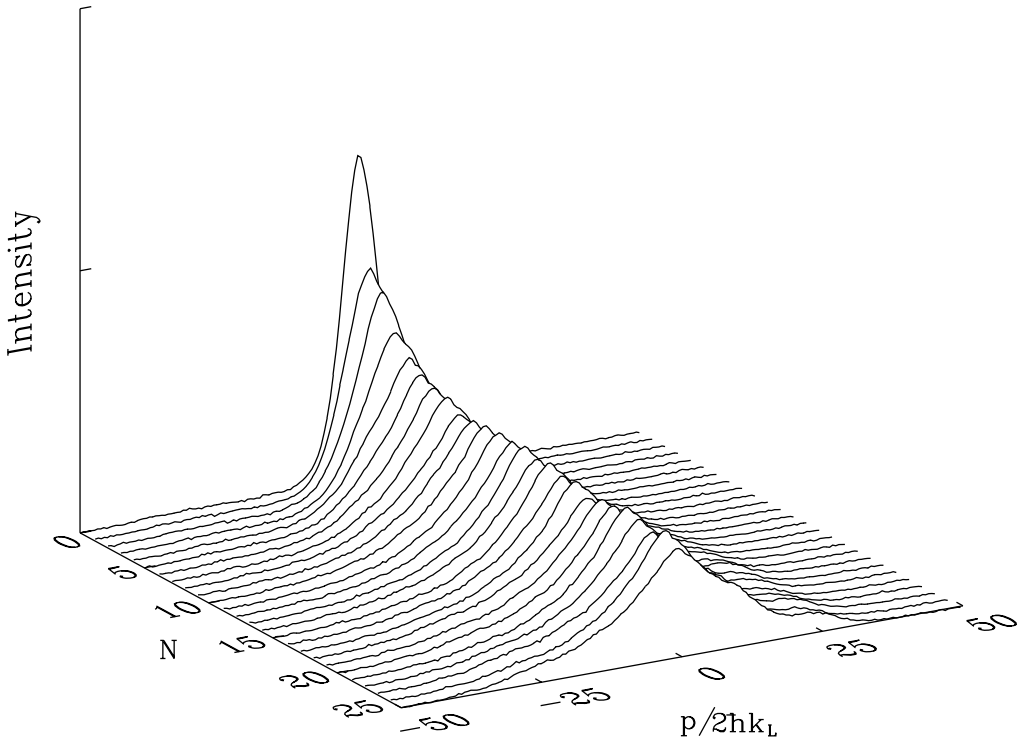

Figure 5.3: Experimental time evolution of the momentum distribution from the initial Gaussian until the exponentially localized distribution. The break time is approximately 8 kicks. Fringes in the freezing molasses lead to small asymmetries in some of the measured momentum distributions as seen here and in the inset of Fig. 5.4. The vertical scale is measured in arbitrary units and is linear.

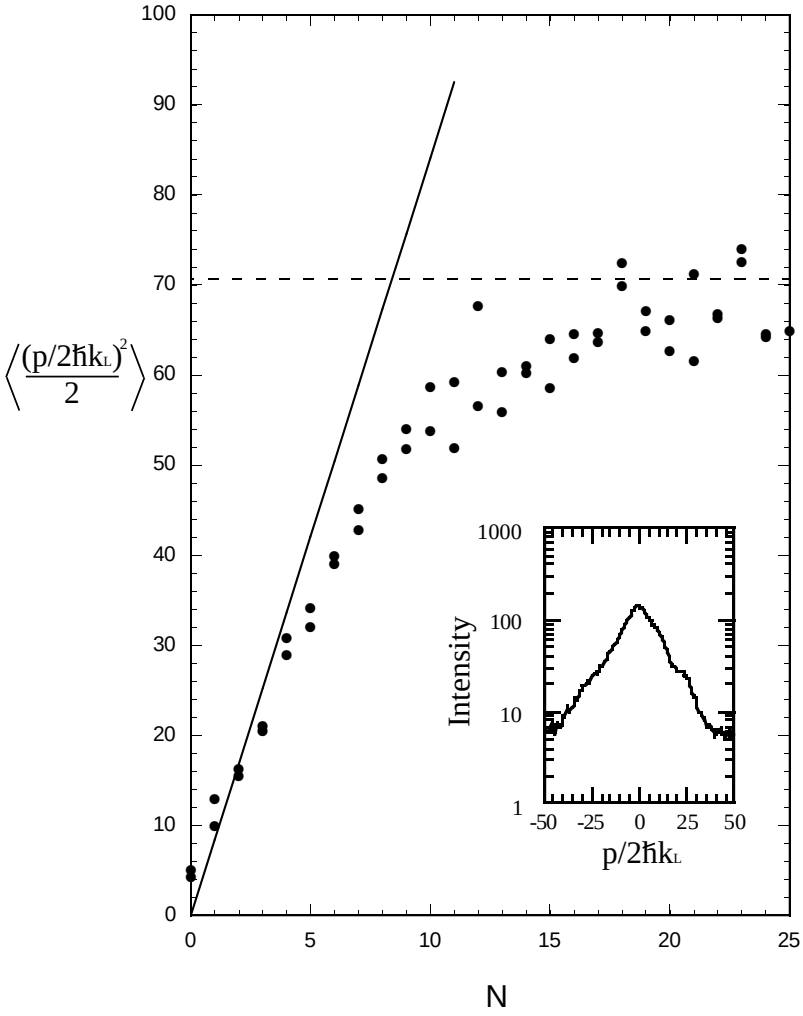

Figure 5.4: Energy $\langle (p/2\hbar k_L)^2 \rangle / 2$ as a function of the number of kicks. The solid dots are the experimental results. The solid line shows the calculated linear growth from the classical dynamics. The dashed line is the saturation value computed from the theoretical localization length ξ. The inset shows an experimentally measured exponential distribution on a logarithmic scale that is consistent with the theoretical prediction.

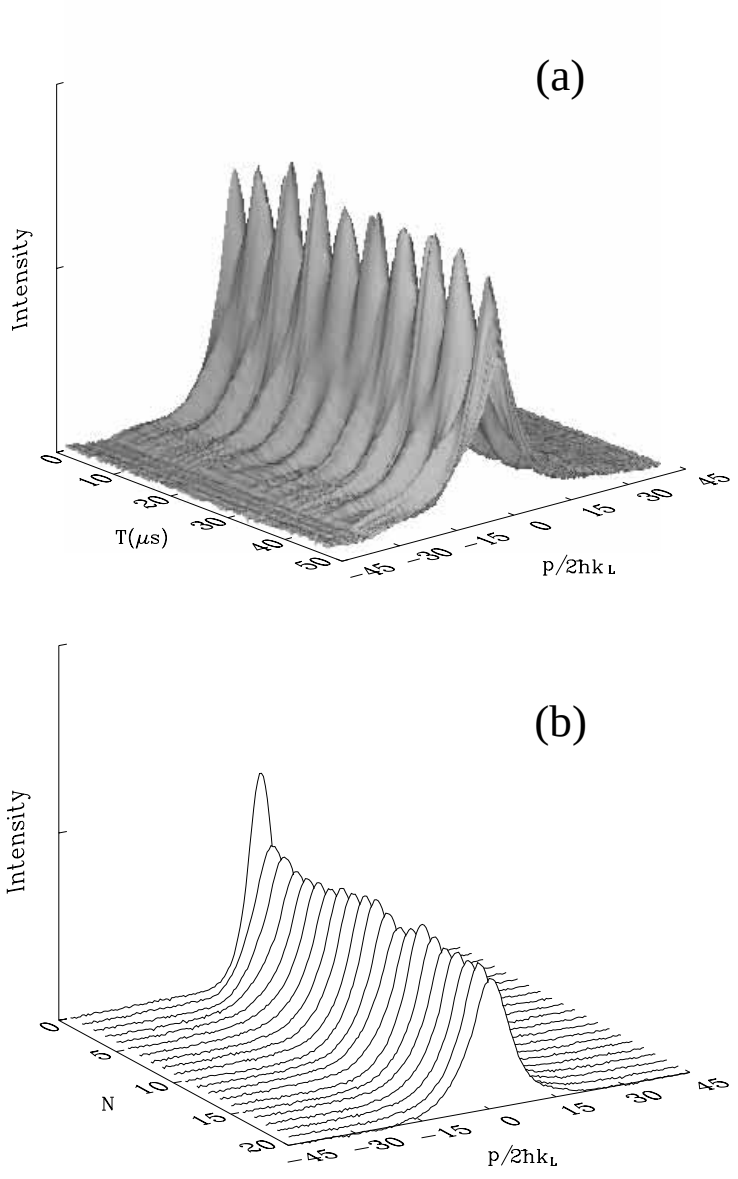

Figure 5.5: Experimental observation of quantum resonances: (a) Occurrence as a function of the period of the pulses. The surface plot is constructed from 150 momentum distributions measured, for each T, after 25 kicks. This value of N ensures that the momentum distributions are saturated for the entire range of T shown. On resonance, the profiles are non-exponential and narrower than the localized distributions that appear off-resonance. Note that the vertical scale is linear. (b) Time evolution of a particular resonance ($T = 10$ μs).

Chapter 6

The Modulated Standing Wave

6.1 Introduction

We now consider subjecting atoms to a standing wave of near-resonant light, where the displacement of the standing wave nodes is modulated at a frequency ω_m and with an amplitude ΔL. Once again, a large detuning is used to eliminate the upper level dynamics of the two-level-atom model. With this form of the modulation [38] the effective Hamiltonian (Eq. 2.7) becomes

$$H = \frac{p^2}{2M} + V_o \cos[2k_L(x - \Delta L \sin \omega_m t)] \ . \tag{6.1}$$

Although this Hamiltonian may look somewhat different than the delta-kicked rotor, it also displays the phenomenon of dynamical localization, as discussed below.

6.2 Experimental Apparatus

To modulate the phase of the potential, we vary the phase of one of the two laser beams that make the standing wave. The electro-optic modulator EOM4 in Fig. 3.2(b) provided this control. For a phase shift of π at 589 nm, this modulator required an applied voltage of $V_\pi = 271$ V. By applying an oscillating drive $V_{EO} \sin \omega_m t$ we modulated the phase of the beam with an amplitude $\pi V_{EO}/V_\pi$

and gave the phase of the standing wave a time dependence $\lambda \sin \omega_m t$, with $\lambda \equiv 2k_L \Delta L = \frac{1}{2}\pi V_{EO}/V_\pi$. To provide the high voltage ($V_{\rm pp} = 2V_{EO} = 2400$ V) required for the phase shifts in this experiment, the signal was stepped-up in a helical resonator [39]. This resonator was designed so that when connected to the capacitive EOM it formed a tuned circuit that had an input impedance of 50 Ω at a resonance frequency of 1.3 MHz. This was the desired modulation frequency $\omega_m/2\pi$. The circuit had a Q of 108 and the output voltage across the EOM was stepped-up by a factor of 77.

6.3 Classical Analysis

The Hamiltonian of Eq. 6.1 can be expanded as a sum of nonlinear resonances using a Fourier expansion. By expanding the temporal dependence of the potential, we obtain the resonance structure of the system,

$$\begin{aligned} H &= \frac{p^2}{2M} + V_o[J_0(\lambda)\cos 2k_L x \\ &\quad + J_1(\lambda)\cos 2k_L(x - v_m t) + J_{-1}(\lambda)\cos 2k_L(x + v_m t) \\ &\quad + J_2(\lambda)\cos 2k_L(x - 2v_m t) + J_{-2}(\lambda)\cos 2k_L(x + 2v_m t) + \cdots] \\ &= V_o \sum_{n=-\infty}^{\infty} J_n(\lambda)\cos 2k_L(x - n v_m t)\ , \end{aligned} \tag{6.2}$$

where J_n are ordinary Bessel functions, $v_m \equiv \omega_m/2k_L$ is the velocity difference between neighboring resonances, and $\lambda = 2k_L\Delta L$ is the modulation index.

As in the case of the delta-kicked rotor, the resonances are located at regular intervals in momentum. The amplitudes of these resonances, however, depend on a controllable experimental parameter, the modulation index λ. The dependence on λ allows this system to be tuned between regimes where

the classical dynamics is integrable (for example, $\lambda = 0$) to those in which it is chaotic.

The classical resonances are evenly separated in momentum with central values of

$$p_n = nMv_m \ , \tag{6.3}$$

and widths of

$$\Delta p_n = 4\sqrt{MV_o|J_n(\lambda)|} \ . \tag{6.4}$$

There are substantial resonances only for $n \leq \lambda$, so for momenta greater than $M\lambda v_m$ the phase space is characterized by essentially free evolution. These regions of free evolution confine the motion of atoms with small initial momentum to the portion of phase space spanned by the resonances. For certain ranges of λ, these resonances overlap, leading to a band of chaos with boundaries in momentum that are proportional to λ. A sample of atoms starting with initial conditions within this band will remain within it, confined to momenta in the range $\pm M\lambda v_m$. A simple estimate of the atomic momentum after a long time is a uniform distribution within these bounds [38]; such a distribution would have an RMS momentum of

$$\frac{p_{\text{RMS}}}{2\hbar k_L} = \frac{M\lambda v_m}{\sqrt{3}\,2\hbar k_L} = \frac{\lambda}{\sqrt{3}}\,\frac{\omega_m}{8\omega_r} \ . \tag{6.5}$$

The classical dynamics also can be understood in terms of resonant kicks that occur twice during each modulation period. Consider an atom subjected to the modulated standing wave of Eq. 6.1. When the standing wave is moving with respect to the atom, the time-averaged force is zero, since the sign of the force changes as the atom goes over "hill and dale" of the periodic potential.

Momentum is transferred to the atom primarily under conditions when the standing wave is stationary in the rest frame of the atom. These resonant kicks occur twice in each modulation period, but they are not equally spaced in time; they occur when the velocity of the standing wave $\lambda v_m \cos(\omega_m t)$ matches that of the atom. The magnitude and direction of the resonant kick depends on where the atom is located within the standing wave at that time.

As shown in the simulation in Fig. 6.1, the most significant changes in the momentum distributions occur during these kicks. The boundary in momentum can be understood from this picture, since for each value of λ there is a maximum velocity of the standing wave. Once an atom is moving faster than this maximum velocity, the resonant kicks cannot occur, and the atom is essentially free.

The calculated variation of the RMS momentum width as a function of λ is shown in Fig. 6.2 for $\omega_m/2\pi = 1.3$ MHz and $V_o/h = 3.1$ MHz. The estimate of Eq. 6.5 is shown by the solid line. For values of $\lambda < 3$, this estimate agrees roughly with an integration of the classical Hamilton's equations [2] (shown in the figure) calculated for an interaction time of 20 μs. For larger values of λ, the simulation is lower than the estimate, because in only 20 μs the initial distribution (with $p_{\mathrm{RMS}}/2\hbar k_L \sim 2.3$) does not have time to diffuse up to the limit represented by the solid line. Except for values of λ close to 7.0 (explained below), the longer-duration classical simulation presented in the figure agrees with the estimate over the entire range of λ shown. The 20 μs classical simulation also shows oscillations in the diffusion rate as a function of λ: peaks in the RMS momentum correspond to values of λ leading to large diffusion rates, while dips indicate slow diffusion.

To understand this variation in diffusion rates, we examine the resonances in Eq. 6.2. The dependence of the diffusion rate on λ is due to oscillations in $J_n(\lambda)$, the amplitudes of the resonances. The variation of these amplitudes is shown in Fig. 6.3. The various resonances grow and shrink as the modulation index λ is increased. For certain values of λ, a resonance can be significantly diminished, or even removed in the case where λ is a zero of one of the Bessel functions. As shown in the computer-generated phase portraits of Fig. 6.4 (top panel), this variation in the amplitudes of the resonances strongly influences the dynamics of the system. In general, the phase spaces are mixed, with islands of stability surrounded by regions of chaos. Atoms from the initial distribution that are contained within an island remain trapped, while those in the chaotic domain can diffuse out to the boundaries. In the case of a diminished resonance, the islands of stability from neighboring resonances might not be destroyed by resonance overlap. This is the case with $\lambda = 3.8$, for which $J_1(\lambda)$ has its first zero. The final momentum spread in this case is governed largely by the surviving island due to the resonance at $p_0 = 0$, and the system is nearly integrable. The stability of this system causes the reduced diffusion shown by the dip in the classical simulation of Fig. 6.2 at $\lambda = 3.8$. Indeed, all of the dips in this simulation occur at values of λ that are near zeroes of Bessel functions; the dynamics of the corresponding systems are stabilized by the diminished resonances. This stabilization even affects diffusion in the long-time classical simulation: for values of λ close to 7.0 (the second zero of $J_1(\lambda)$), the initial conditions are trapped in a large island of stability at $p = 0$. For these values of λ, the diffusion is limited by the width of the island to a value much smaller than that given by the resonant-kick boundary.

Note that the oscillations of the Bessel functions are reflected in the exchange of the location of hyperbolic and elliptic fixed points. At $\lambda = 0$, there is only one resonance in the expansion of Eq. 6.2 centered at $p_0 = 0$ with an amplitude $V_o\, J_0(0) = +V_o$. The potential minima for this resonance are located in space at even multiples of $\pi/2k_L$, so the island of stability is centered at $x = 0$ in the phase portrait. The phase portraits for $\lambda = 3$ and $\lambda = 3.8$ also have islands of stability centered in momentum at $p_0 = 0$, but the amplitudes for these resonances are negative: $V_o\, J_0(3) = -0.40\, V_o$, and $V_o\, J_0(3.8) = -0.26\, V_o$. The reversal of sign exchanges the location of the potential minima and maxima, so the islands in these portraits are centered in position at $x = \pi/2k_L$.

Notice also that the overall amplitude of the oscillations decreases as λ is increased due to the reduction in the size of each resonant-kick. This effect can be understood from the impulse approximation, since the maximum classical force is fixed but the time that the standing wave potential is stationary in the rest frame of the atom is inversely proportional to λ. The classical diffusion rate is therefore reduced by increasing λ, although the classical saturation value of p_{RMS} increases with λ.

6.4 Experimental Results: Quantum Mechanical Effects

Also shown in Fig. 6.2 are experimental data points (diamonds) for interaction times of 10 and 20 μs. The 20 μs data match the classical simulations well for small values of λ and for values of λ that are close to zeroes of Bessel functions. For other values of λ, however, the experimentally measured distributions are much narrower than those predicted classically. What causes this reduction in the width of the observed momentum distributions?

As discussed in Chapter 5, it is well known that classically diffusive behavior can be suppressed quantum mechanically by a mechanism analogous to Anderson localization [28]. Referred to as dynamical localization, this mechanism predicts saturation in the energy transfer (momentum, in our case) and a resulting exponential distribution with a characteristic localization length ξ (in momentum). In the experiments, we have to ensure that the location of the resonant-kick boundary is much further than ξ to observe this distribution. As this boundary scales linearly with λ, we expect to see the appearance of dynamical localization only beyond some value of λ. This experimental requirement is similar to the considerations of the classical boundary in the delta-kicked rotor experiments. There, however, the boundary was due to an effective reduction in K by the motion of an atom over several wells during a single pulse. Here the classical boundary arises from the maximum velocity that can be imparted to an atom by resonant kicks.

In Fig. 6.2 the empty and solid diamonds are experimental data for two different interaction times showing that these results are close to saturation for the range of λ shown. Note that for small values of λ there is good agreement with the classical prediction. At $\lambda = 0$ the system is integrable and momentum is trivially localized. As λ is increased the phase space becomes chaotic, but growth is limited by the resonant-kick boundary. Our measured momentum distributions (in Fig. 6.4, bottom panel) are characteristically "boxlike" in this regime ($0 \leq \lambda \leq 2$). This observation is consistent with the picture of a uniform diffusion limited by the boundaries in momentum.

As λ is increased beyond a critical value, there are oscillations in the observed RMS momentum. For certain ranges of the modulation index λ, the ob-

served values deviate substantially from the classical prediction. These ranges correspond to conditions of large diffusion rates — the peaks in the classical prediction. For these values of λ the classical phase space is predominately chaotic. An example of the resulting dynamics is shown in Fig. 6.4 for $\lambda = 3.0$. The classically predicted distribution (middle panel) is roughly uniform, but the experimentally observed distribution is exponentially localized [1, 2]; hence the RMS value is reduced. As in the experiments of Chapter 5, this result is an observation of dynamical localization.

As λ is increased further, the oscillations in the resonance amplitudes lead to phase portraits with large islands of stability, as in the case $\lambda = 3.8$. For these values of λ the classical phase space becomes nearly integrable and the measured momentum is close to the classical prediction.

Quantum analyses under the conditions of the experiment as well as an asymptotic (long-time limit) Floquet analysis [12] are shown along with the classical simulations and experimental data in Fig. 6.2. The predicted distributions from the Floquet analysis are displayed along with the experimentally observed ones in the lower panel of Fig. 6.4. It is clear that there is good quantitative agreement between experiment and the effective single particle analysis [2, 40].

The modulated system is characterized in general by a mixed phase space. In certain regimes, such as for $\lambda = 3.0$, the stable regions become very small and dynamical localization can be observed. The main focus for future work with the modulated system is, however, the study of quantum dynamics in a mixed phase space. These experiments will require better-defined initial conditions that are localized in position as well as in momentum, and will be

the main emphasis of a cesium-based experiment that is now being constructed in our laboratory.

Mixed phase space dynamics inherently complicate the analysis of dynamical localization and it is useful to realize a system where the chaos is more widespread. Also, there is a characteristic time scale, the "quantum break time", beyond which the saturation effects of dynamical localization are predicted to occur. With a further modification of the basic experimental setup, we can both realize globally chaotic behavior and track the time evolution of the localization phenomena.

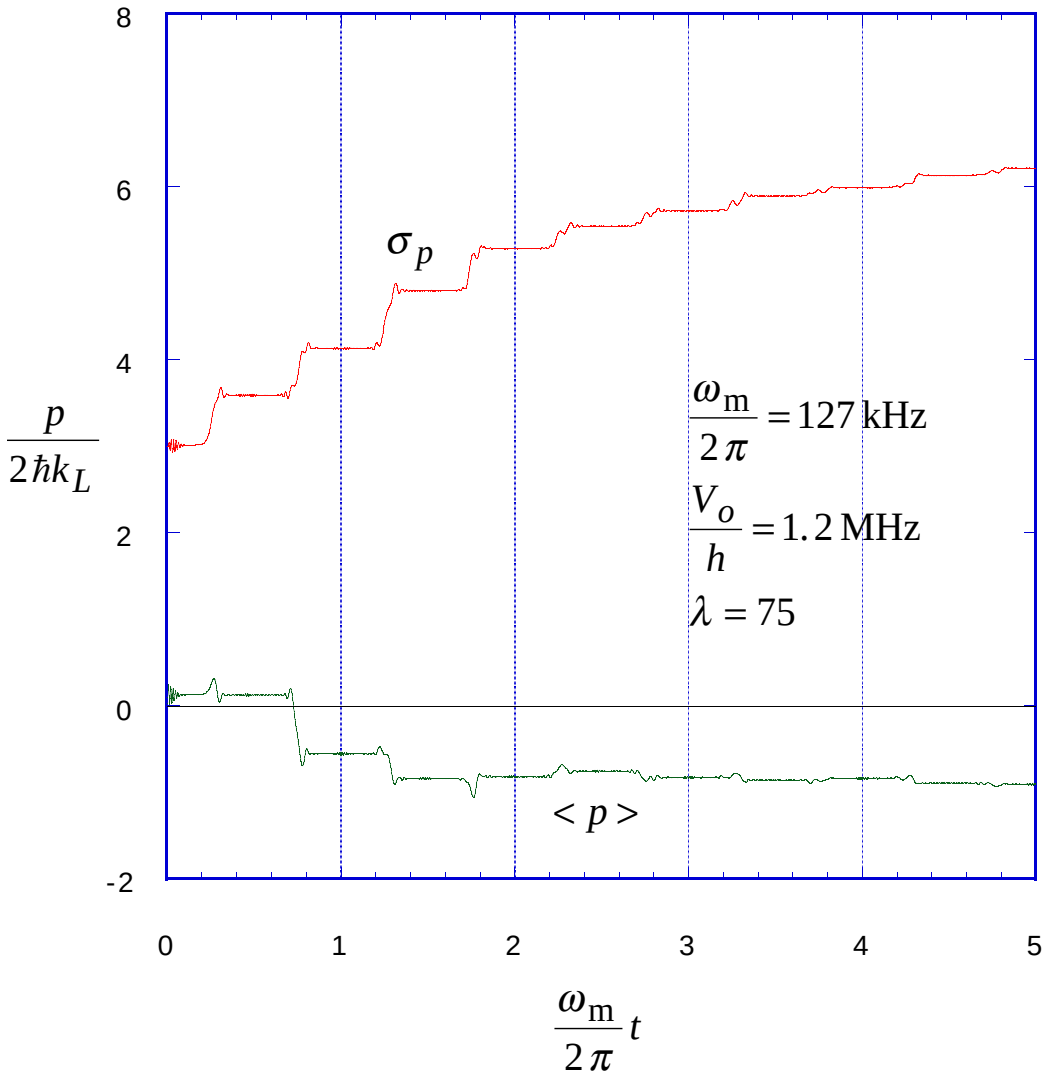

Figure 6.1: Simulation of resonant kicks. This quantum simulation tracks the evolution of a Gaussian wavepacket exposed to the Hamiltonian of Eq. 6.1. The mean and RMS widths of the resulting wavepacket's momentum distribution are plotted here as a function of time. Twice during each modulation period the atomic wavepacket is subjected to a resonant kick. The most significant changes in momentum occur during these kicks. In this simulation, the wavepacket's initial width in momentum was $\sigma_{po}/2\hbar k_L = 3$.

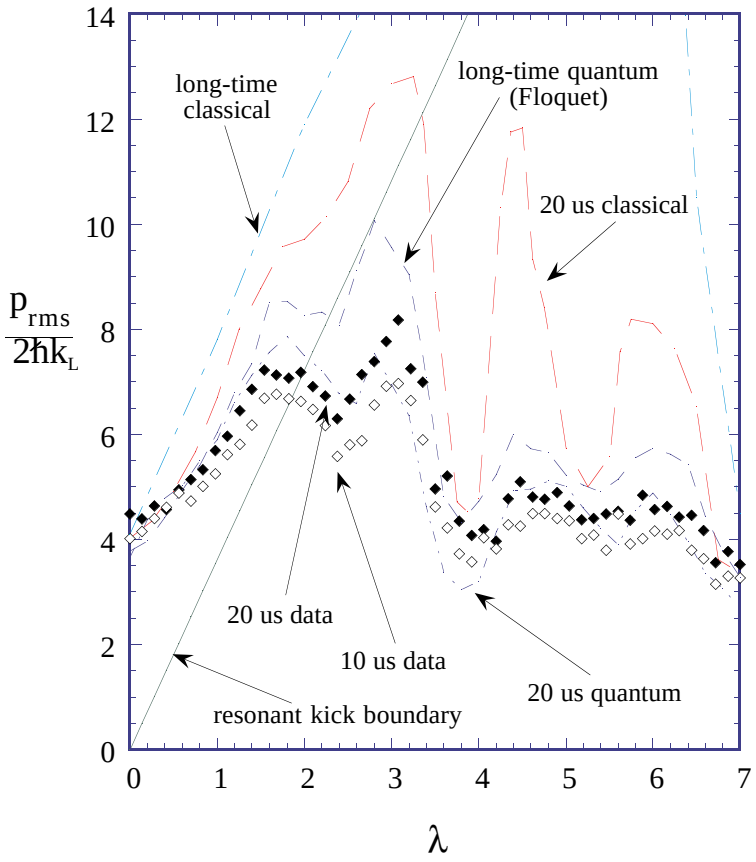

Figure 6.2: RMS momentum width as a function of the modulation amplitude λ, for $\omega_m/2\pi = 1.3$ MHz and $V_o/h = 3.1$ MHz. Experimental data are denoted by diamonds and have a 10% uncertainty associated with them. The empty diamonds are for an interaction time of 10 μs and the solid diamonds are for 20 μs. The straight line denotes the resonant-kick boundary. The four curves indicate numerical simulations. Two integrations of the classical model are shown, one for a simulation time of 20 μs, and one for the long time limit that shows the maximum diffusion in momentum. The observed data lie well below these curves for some values of λ. A 20 μs integration of the Schrödinger equation is also presented for comparison with the corresponding experimental data. Also shown is a long-time quantum calculation in which the system's solution was found in terms of its Floquet states.

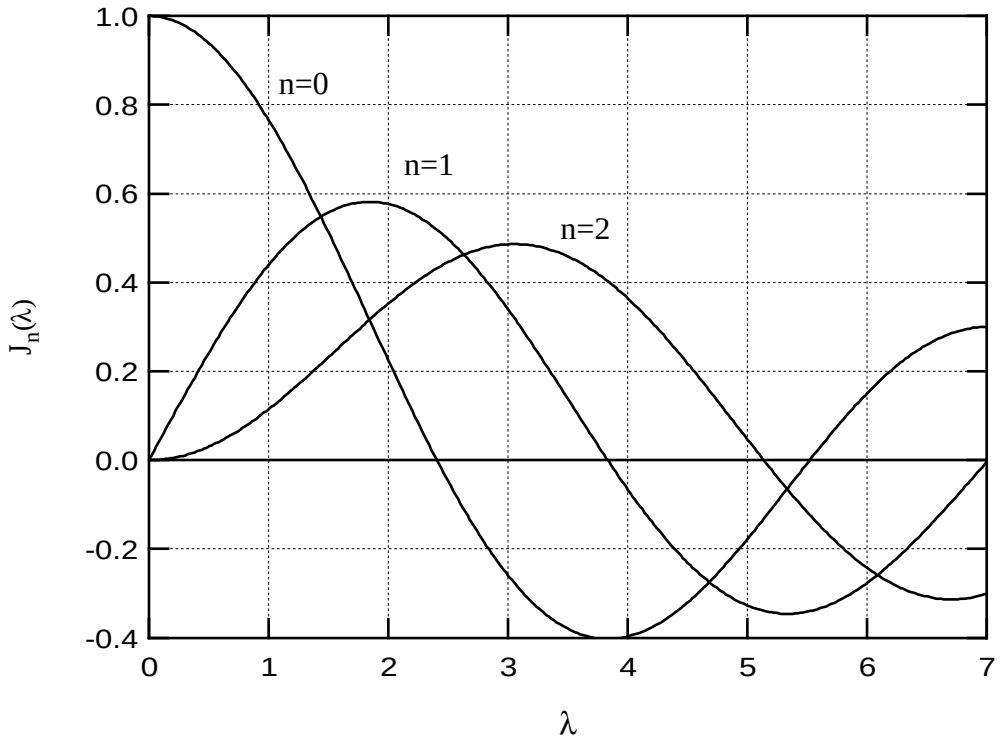

Figure 6.3: The first three ordinary Bessel functions. The oscillations of these functions lead to oscillations in the widths of resonances in the modulated system.

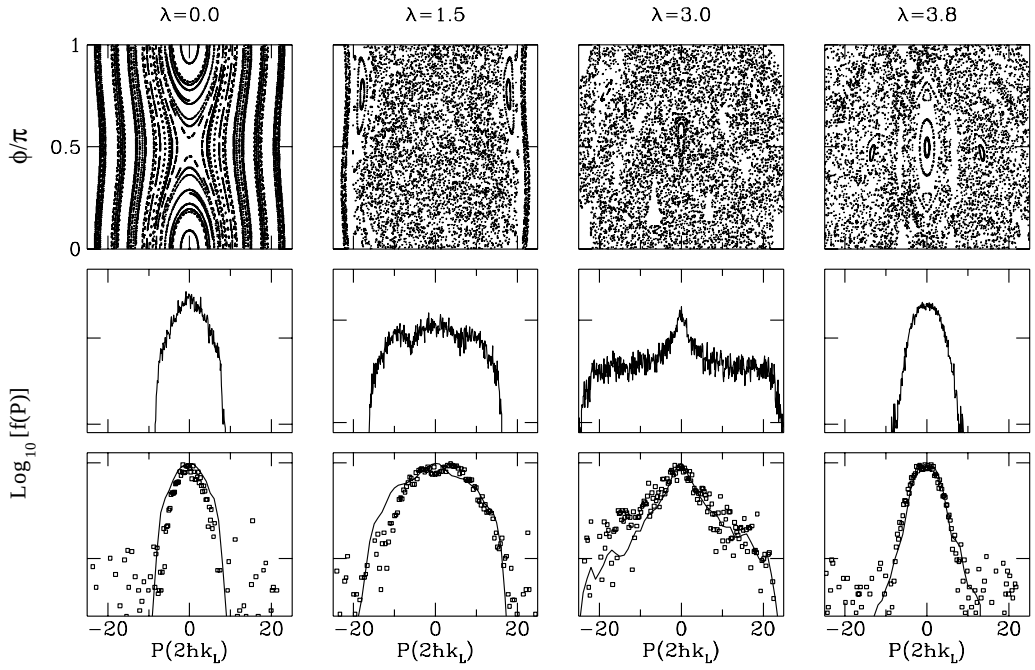

Figure 6.4: Poincaré surfaces of section (upper panel), classical momentum distributions (middle panel), and experimentally measured momentum distributions with Floquet theory (bottom panel, theory marked by lines) for runs with parameters similar to those in Fig. 6.2. Note that the vertical scales for the distributions are logarithmic and are marked in decades.

Chapter 7

Future Directions

This work establishes a new experimental testing ground for quantum chaos, in which it should be possible to study many aspects of this field. These experiments introduce a method of studying $1-D$ quantum systems with virtually ideal spatial periodicity and no noise. The experiments allow direct comparisons to theoretical predictions with no adjustable parameters, and direct control over all experimental parameters.

Some topics for future study include noise-induced delocalization [41, 42] and localization in two and three dimensions [32]. Using recently developed techniques of atom cooling and manipulation it should be possible to prepare the atoms in a localized region of phase space. This state preparation technique would enable a detailed study of quantum transport in mixed phase space. Other interesting topics to study would be tunneling from islands of stability, chaos-assisted tunneling, and quantum scars [43].

Bibliography

[1] F. L. Moore, J. C. Robinson, C. Bharucha, P. E. Williams, and M. G. Raizen, *Phys. Rev. Lett.* **73**, 2974 (1994).

[2] J. C. Robinson, C. Bharucha, F. L. Moore, R. Jahnke, G. A. Georgakis, Q. Niu, M. G. Raizen, and Bala Sundaram, *Phys. Rev. Lett.* **74**, 3963 (1995).

[3] F. L. Moore, J. C. Robinson, C. F. Bharucha, Bala Sundaram, and M. G. Raizen, *Phys. Rev. Lett.* **75**, 4598 (1995).

[4] J. C. Robinson, C. F. Bharucha, K. W. Madison, F. L. Moore, Bala Sundaram, S. R. Wilkinson, and M. G. Raizen, *Phys. Rev. Lett.* **76**, 3304 (1996).

[5] This work was reviewed in "Search and Discovery," Graham P. Collins, *Physics Today* June 1995, p. 18.

[6] John C. Robinson, Ph.D. Dissertation, The University of Texas at Austin, 1995.

[7] S. R. Wilkinson, C. F. Bharucha, K. W. Madison, Qian Niu, and M. G. Raizen, *Phys. Rev. Lett.* **76**, 4512 (1996).

[8] C. F. Bharucha, K. W. Madison, P. R. Morrow, S. R. Wilkinson, Bala Sundaram, and M. G. Raizen, *Phys. Rev. A* **55**, R857 (1997).

[9] S. R. Wilkinson, C. F. Bharucha, M. C. Fischer, K. W. Madison, P. R. Morrow, Qian Niu, Bala Sundaram, and M. G. Raizen, To appear in *Nature*.

[10] Patrick R. Morrow, Ph.D. Dissertation, The University of Texas at Austin, 1996.

[11] Martin C. Fischer, Master's Thesis, The University of Texas at Austin, 1993.

[12] Georgios A. Georgakis, Ph.D. Dissertation, The University of Texas at Austin, 1996.

[13] *Irregular Atomic Systems and Quantum Chaos*, J. C. Gay, ed. (Gordon and Breach, New York, 1992).

[14] R. V. Jensen, *Nature* (London) **355**, 311 (1992).

[15] H. Friedrich and D. Wintgen, *Phys. Reps.* **183**, 37 (1989); D. Delande in *Chaos and Quantum Physics*, M.-J. Giannoni, A. Voros and J. Zinn-Justin, eds. (Elsevier, London, 1991).

[16] P. M. Koch and K. A. H. van Leeuwen, *Phys. Reps.* **255**, 289 (1995).

[17] G. S. Ezra, K. Richter, G. Tanner and D. Wintgen, *J. Phys. B* **24**, L413 (1991).

[18] See, for example, contibutions in *Physica D* **83** (1995).

[19] See, for example, *Quantum chaos: between order and disorder: a selection of papers*, G. Casati and B. V. Chirikov, eds. (Cambridge University Press, New York, 1995).

[20] Laser cooling and trapping is reviewed by Steven Chu in *Science* **253**, 861 (1991).

[21] C. S. Adams, M. Sigel, and J. Mlynek, *Phys. Reps.* **240**, 145 (1994).

[22] C. Cohen-Tannoudji, in *Fundamental Systems in Quantum Optics*, Les Houches, 1990, J. Dalibard, J. M. Raimond and J. Zinn-Justin, eds. (Elsevier, London, 1992).

[23] Cyrus Bharucha, Master's Thesis, The University of Texas at Austin, 1994.

[24] E. Raab, M. Prentiss, A. Cable, S. Chu, and D. Pritchard, *Phys. Rev. Lett.* **59**, 2631 (1987).

[25] See, for example, P. J. Martin, P. L. Gould, B. G. Oldaker, A. H. Miklich, and D. E. Pritchard, *Phys. Rev. A* **36**, 2495 (1987).

[26] B. V. Chirikov, *Phys. Reps.* **52**, 265 (1979).

[27] G. H. Walker, and J. Ford, *Phys. Rev.* **188**, 416 (1969).

[28] L. E. Reichl, *The Transition to Chaos in Conservative Classical Systems: Quantum Manifestations.* (Springer-Verlag, Berlin, 1992).

[29] R. Blümel, S. Fishman, and U. Smilansky, *J. Chem. Phys.* **84**, 2604 (1986).

[30] Michael Tabor, *Chaos and Integrability in Nonlinear Dynamics.* (Wiley, New York, 1989).

[31] A. L. Lichtenberg and M. A. Lieberman, *Regular and Chaotic Dynamics.* (Springer-Verlag, Berlin, 1991).

[32] Giulio Casati, Italo Guarneri, and D. L. Shepelyansky, *Phys. Rev. Lett.* **62**, 345 (1989).

[33] B. Chirikov, F. M. Izrailev, and D. L. Shepelyansky, *Sov. Sci. Rev. Sec. C* **2**, 209 (1981).

[34] D. L. Shepelyansky, *Phys. Rev. Lett.* **56**, 677 (1986); *Physica D* **28**, 103 (1987).

[35] M. G. Raizen, Bala Sundaram, and Qian Niu, *Phys. Rev. Lett.* **78**, 1194 (1997).

[36] F. M. Izrailev, and D. L. Shepelyansky, *Sov. Phys. Dokl.* **24**, 996 (1979); *Theor. Math. Phys.* **43**, 553 (1980).

[37] Q. Niu and Bala Sundaram, to be submitted for publication.

[38] R. Graham, M. Schlautmann, and P. Zoller, *Phys. Rev. A* **45**, R19 (1992).

[39] W. W. Macalpine, R. O. Schildknecht, *Proc. of the IRE*, 2099 (1959).

[40] P. J. Bardroff, I. Bialynicki-Birula, D. S. Krähmer, G. Kurizki, E. Mayr, P. Stifter, and W. P. Schleich, *Phys. Rev. Lett.* **74**, 3959 (1995).

[41] T. Dittrich and R. Graham, *Europhys. Lett.* **4**, 263 (1987).

[42] S. Fishman, and D. L. Shepelyansky, *Europhys. Lett.* **16**, 643 (1991).

[43] E. J. Heller, and S. Tomsovic, *Physics Today*, July 1993, p. 38.

Vita

Following his only sibling, Jyoti, by fifteen minutes, Cyrus Bharucha was born to Farrokh and Laju Bharucha in Bristol on the thirteenth of August, 1967. Three years later the family moved to the United States, where the children were taught to value education in the tradition of their Indian heritage.

After graduating from Cardinal Gibbons High School in Fort Lauderdale, Cyrus earned his Bachelor's degrees in Biophysics and Electrical Engineering at Rice University. He entered The University of Texas at Austin in August 1991. In Professor Mark Raizen's laboratory he participated in experimental and theoretical work on quantum chaos (described in this dissertation), atom interferometry, and quantum transport in optical lattices.

One of Cyrus' favorite pastimes is swimming and he is a big fan of Austin's Barton Springs. He also enjoys film, ballroom dance, travel, and flying.

Permanent address: 7823 Sandspoint
Houston, Texas 77036

bharucha.com

This Dissertation was typeset with LaTeX[‡] by the author.

[‡]LaTeX is a document preparation system developed by Leslie Lamport as a special version of Donald Knuth's TeX Program.